Neuroligin-2 is ubiquitinated by Nedd4l to control developmental astrocyte morphogenesis.

Kristina Sakers[1-2*], Juan J. Ramirez[1,3], Nimrod Elazar[1-2], Leykashree Nagendren[1], Erik Soderblom[1, 3], Cagla Eroglu[1-2,4]

Affiliations:

1. Department of Cell Biology, Duke University Medical Center, Durham, NC, USA
2. Howard Hughes Medical Institute, Duke University Medical Center, Durham, NC, USA
3. Duke Proteomics and Metabolomics Shared Resource and Duke Center for Genomic and Computational Biology, Duke University Medical School, Durham, North Carolina, USA
4. Department of Neurobiology, Duke University Medical Center, Durham, NC, USA

Corresponding Authors:

Kristina Sakers, Ph.D. kristina.sakers@duke.edu

Cagla Eroglu, Ph.D. cagla.eroglu@duke.edu

SUMMARY

Sakers et al report that astrocytic neuroligins (NLs) are functionally diverse proteins, with unique intracellular protein-protein interactions. They show that Nedd4l binds to NL2 and ubiquitinates its intracellular domain, leading to changes in NL2 stability. In vivo, Nedd4l and NL2 ubiquitination are critical for astrocyte morphogenesis.

ABSTRACT

Central nervous system astrocytes have an intricate, highly branched morphology. Proper development of perisynaptic astrocyte processes is necessary for tripartite synapse formation and function. However, cellular pathways orchestrating this development are largely unknown. Neuroligins (NLs) 1-3 regulate astrocyte morphogenesis via transcellular adhesions with neuronal neurexins. Here, we found an astrocytic NL2-based mechanism governing morphogenesis. Through structure and function studies, we identified a WW-binding motif within the NL2 intracellular domain required for astrocyte morphogenesis. Using cell-specific *in vivo* proximity labeling (iBioID), we found that each NL displays distinct protein-protein interactions within astrocytes, distinct from the neuronal NL2 binding partners. From these data, we identified a role for WW domain-containing E3 ubiquitin ligase Nedd4l in astrocyte morphogenesis. Biochemical assays revealed Nedd4l ubiquitinates and stabilizes NL2, and this ubiquitination is required for astrocyte morphogenesis. This study shows that Neuroligins have non-overlapping roles in controlling astrocyte growth and uncovers a molecular mechanism of how NL2 mediates astrocyte morphogenesis.

INTRODUCTION

Protoplasmic astrocytes of the central nervous system (CNS) have a unique bush-like morphology. The molecular mechanisms that govern how astrocytes develop their complex structure are largely unknown. Astrocytes tile the brain and extend fine filopodia-like processes into the neuropil (Bushong et al., 2004, 2002), facilitating an active role in critical brain functions, including synaptogenesis, regulation of synaptic strength, and buffering of neurotransmitters and ions (Farizatto and Baldwin, 2023; Verkhratsky and Nedergaard, 2018). Human astrocytes are disproportionately larger and more complex than rodent astrocytes (Oberheim et al., 2006), suggesting that higher-order species require astrocytes for advanced brain function. Consequently, astrocyte dysfunction has been identified across a myriad of neurological diseases (Tian et al., 2010; Rothstein et al., 1995; Preman et al., 2021; Booth et al., 2017; Gutmann et al., 1999). In particular, a recent study found that numerous Alzheimer's risk genes correlate specifically with astrocyte territory size (Endo et al., 2022). Thus, it is crucial to understand how astrocyte morphogenesis proceeds and which cell biological mechanisms govern this process.

Various signals have emerged as regulators of astrocyte growth, including the neuron-derived secreted factors Sonic Hedgehog (Xie et al., 2022) and BDNF (Holt et al., 2019), actin-binding proteins such as Ezrin (Endo et al., 2022; Lavialle et al., 2011; Wang et al., 2025) and Profilin-1 (Molotkov et al., 2013), and numerous cell-adhesion molecules (Baldwin et al., 2023). Among the latter, Neuroligins (NLs) play a critical role in the morphogenesis of astrocytes (Ackerman et al., 2021; Stogsdill et al., 2017), as well as oligodendrocyte precursor cells (Li et al., 2024). NLs are trans-synaptic cell-

adhesion proteins that bind to Neurexins to promote synaptic formation (Barrow et al., 2009; Chih et al., 2005; Scheiffele et al., 2000; Shipman and Nicoll, 2012) and function (Babaev et al., 2016; Varoqueaux et al., 2006). There are four NL genes expressed in rodents, with NL1, NL2, and NL3 being the predominantly expressed family members. In rodent neurons, NL1 dose-dependently controls dendritic morphology, with NL1 overexpression increasing and NL1 knockdown decreasing dendritic arborization (Schnell et al., 2014, 2012). In contrast, loss of NL3 results in a more complex dendritic arbor (Xu et al., 2019), suggesting non-overlapping roles for NLs in controlling neuronal morphology. Neuronal NLs also have non-redundant roles in controlling synaptic function (Chanda et al., 2017; Nguyen et al., 2016). In astrocytes, loss of NLs 1-3 each reduces astrocyte territory and neuropil infiltration size (Stogsdill et al., 2017). However, whether NLs play unique roles in astrocyte morphogenesis and what mechanisms control this process is unclear. NLs are implicated in neurodevelopmental diseases, including Autism Spectrum Disorder (Jamain et al., 2003; Parente et al., 2017), and thus, it is imperative to understand NL function across all cell types throughout development.

Functional differences across NLs may stem from amino acid sequence divergence. Rodent NLs 1-3 have similar extracellular domains (ECD, ~75% homology) and more disparate intracellular domains (ICD, ~50% homology). Several amino acid motifs in NL ICDs have been shown to direct interactions with specific protein partners, ultimately leading to unique functional consequences such as the specification of inhibitory versus excitatory synapses (Poulopoulos et al., 2009; Shipman et al., 2011; Sumita et al., 2007). One study using chimeric NLs demonstrated that NL function is not solely

84 dependent on Neurexin binding to the ECD, but also requires interactions with
85 intracellular proteins to control synapse-specific functions (Nguyen et al., 2016). Further,
86 post-translational modifications on NL ICDs can influence protein-protein interactions
87 and downstream signaling. For example, NL1 tyrosine phosphorylation at Y782 results
88 in preferential binding to the excitatory postsynaptic protein PSD-95 over the inhibitory
89 postsynaptic scaffold protein Gephyrin. PSD95 then recruits α-amino-3-hydroxy-5-
90 methyl-4-isoxazolepropionic acid (AMPA) receptors and controls synaptic firing
91 (Giannone et al., 2013; Letellier et al., 2018). These studies have been conducted in a
92 neuronal context; thus, whether astrocytic NLs exhibit distinct protein-protein
93 interactions and how these interactions control astrocyte development remain unknown.

94 In this study, we show that NLs 1-3 are not redundant in controlling astrocyte
95 morphological development. We identify that the WW-binding motif in NL2 is necessary
96 for astrocyte morphogenesis. Using an unbiased *in vivo* proximity-labeling approach, we
97 uncover interaction networks for astrocytic NL1, NL2, and NL3. We also performed
98 proximity labeling of neuronal NL2 to compare cell-type-specific differences in its
99 interactome and function. We show that NLs have distinct interactomes representing
100 unique functions within astrocytes and between astrocytes and neurons. These data
101 reveal numerous WW-domain-containing proteins that are putative interactors of WW
102 motifs in NLs. Of these, we identified Nedd4l, a HECT-domain E3 ubiquitin ligase, to
103 control NL2 stability via ubiquitination, which is necessary for astrocyte morphogenesis.
104 Moreover, the loss of Nedd4l in astrocytes results in a stunted astrocyte morphology.
105 Importantly, Nedd4l interacts with NL1 and NL2, but not NL3. Together, this study

106 reveals unique interactions of astrocytic NL2, providing a previously unknown

107 mechanism for astrocyte morphological development.

108 **RESULTS**

109 **Astrocytic Neuroligins 1, 2, and 3 have non-redundant roles in morphogenesis.**

110 NLs 1, 2, and 3 are all expressed throughout development in mouse cortical astrocytes
111 (Boisvert et al., 2018; Clarke et al., 2018; Zhang et al., 2014; Farhy-Tselnicker et al.,
112 2021). Loss of either NL1, NL2, or NL3 from cortical astrocytes significantly reduces
113 astrocyte complexity, and the loss of all three NLs together results in an additive
114 reduction of complexity (Stogsdill et al., 2017), indicating that these proteins play distinct
115 roles during astrocyte development. NLs have similar ECD amino acid sequences yet
116 differ substantially in their intracellular domains (Fig 1A). Given differences in amino
117 acid sequences and the combinatorial deficit in astrocyte complexity, we examined
118 whether NLs have redundant roles in astrocyte morphogenesis. To do so, we used an
119 optimized and validated *in vitro* astrocyte-neuron co-culture method to quantify
120 astrocyte branch complexity via Sholl analysis (Stogsdill et al., 2017; Baldwin et al.,
121 2021; Tan et al., 2023) (Fig 1B). In this *in vitro* system, astrocytes require neuronal
122 contact to develop a highly branched morphology (Baldwin et al., 2021; Stogsdill et al.,
123 2017) and we can manipulate astrocyte gene expression without affecting the neurons.
124 Because NL2 loss affects astrocyte morphogenesis *in vivo* at both early and late
125 developmental time points, we focused on this NL. We transfected astrocytes with a
126 plasmid expressing an shRNA for *Nlgn2* (shNL2), which has been validated for NL2
127 knockdown efficiency and NL2 specificity (Fig S1A, B) and extensively tested for off-
128 target effects (Stogsdill et al., 2017; Chih et al., 2006; Singh et al., 2016). This plasmid
129 also encodes CAG-GFP to visualize transfected cells. Loss of *Nlgn2* in astrocytes
130 causes a substantial reduction in astrocyte morphology when co-cultured with neurons

131 (Fig S1C-D; Fig 1C-D). To provide additional evidence for the role of Nlgn2 in astrocyte
132 morphogenesis and to address potentially confounding effects of shRNA toxicity (Goel
133 and Ploski, 2022), we designed and tested gRNAs targeting rat *Nlgn2* (Fig S1E). Two of
134 three of the gRNAs targeting *Nlgn2* caused a translation-disrupting frameshift mutation,
135 reflected by the loss of GFP expression downstream of the gRNA and PAM sequences
136 (see Methods) (Fig S1F). We expressed these gRNAs in primary rat astrocytes, along
137 with *Staphylococcus aureus* Cas9 (SaCas9) (Hunker and Zweifel, 2020), under the
138 control of the GfaABC1D promoter (Lee et al., 2008) and found that both gRNAs
139 significantly reduced the morphological complexity in transfected astrocytes cultured
140 with WT neurons, compared to the empty vector control (Fig S1G, H). These data
141 further support that the morphological phenotype observed in Nlgn2 shRNA-transfected
142 cells cannot be explained by cytotoxicity.

143 Next, we tested whether the stunted morphological phenotype of *Nlgn2* knockdown
144 astrocytes can be rescued by the co-expression of an HA-tagged NL2 that has been
145 modified to be shNL2 resistant (HA-NL2-RM, Fig S1A, B) (Stogsdill et al., 2017) or via
146 the co-expression of HA-tagged NL1 or NL3 with shNL2, to investigate whether
147 increasing total NL levels can compensate for the loss of another. Interestingly, HA-
148 tagged NL1 or NL3 did not rescue the astrocyte morphology (Fig 1C, D). In contrast, co-
149 expression of HA-NL2 with either shNL1 or shNL3 resulted in a higher number of
150 maximum intersections in the astrocyte branches compared to a scrambled shRNA
151 control (shCtrl) (Fig 1E, F). Together, these data show that NLs 1, 2, and 3 do not have
152 redundant roles in controlling astrocyte morphogenesis. Moreover, these findings
153 suggest that NL2 is indispensable in astrocyte morphological development.

154 **The intracellular WW-binding motifs of Neuroligins uniquely regulate astrocyte**
155 **morphology**

156 Previous work has revealed unique roles for NL ICDs in controlling synaptic
157 transmission (Nguyen et al., 2016). Thus, we hypothesized that the ICDs of NLs may
158 underlie their distinct roles in controlling astrocyte morphogenesis. NLs contain multiple
159 protein motifs in their ICDs (Fig S2A) that regulate binding to synaptic scaffolding
160 molecules, including Gephyrin and Collybistin (Poulopoulos et al., 2009), which are
161 necessary for inhibitory synapse specification, and PSD-95 (Irie et al., 1997), which
162 organizes excitatory postsynaptic sites. We wondered if any of these motifs in the NL2
163 ICD are necessary for astrocyte morphology. We used mutagenesis to either: delete the
164 NL2 PDZ binding domain (NL2 ΔPDZ, deletion of amino acids 833-836), delete the NL2
165 polyproline-rich motif, which activates Collybistin (NL2 ΔPRM, deletion of amino acids
166 798-805) or mutate NL2 Gephyrin binding residue (NL2 GBM, Y770A) (Fig 2A). All of
167 these constructs use the HA-NL2-RM sequence to prevent their degradation by shNL2.
168 We tested whether these mutant constructs could rescue the shNL2 morphological
169 deficits in our co-culture system. These mutants were properly trafficked to the cell
170 surface (Fig S2B) and rescued the morphological deficits in shNL2 astrocytes (Fig 2B-
171 C), suggesting that potential interactions with Gephyrin, Collybistin, and PSD-95 are
172 dispensable for NL2 control of astrocyte morphology.

173 To identify the regions of the NL2 ICD that are required for astrocyte morphogenesis,
174 we used previously validated (Nguyen et al., 2016) NL2 chimeric constructs to
175 investigate whether replacing the NL2 ICD with either the NL1 or the NL3 ICD is
176 sufficient to rescue the loss of NL2 in astrocytes (Fig 2D). Using astrocyte-neuron co-

177 cultures, we expressed the NL chimeras (HA-NL2-RM sequence) in astrocytes in the
178 presence of shNL2 and quantified astrocyte complexity (Fig 2E). While the NL2
179 ECD/NL1 ICD condition resulted in more complex astrocytes than shNL2 alone, the
180 astrocytes transfected with NL2 ECD/NL3 ICD were identical to shNL2 alone (Fig 2F).
181 This finding suggests that the NL1 and NL2 ICDs share a common amino acid
182 sequence required for controlling astrocyte morphology, which is absent from the NL3
183 ICD.

184 To pinpoint the interaction motif in the NL2 ICD that is required for astrocyte
185 morphogenesis, we aligned the intracellular domain amino acid sequences of NL1-3
186 (Fig 2G, Fig S2A) and isolated motifs that were present in both NL1 and NL2, but
187 absent from NL3. Using TomTom motif scanning (Gupta et al., 2007), we found the
188 sequence PPDY – a Group I WW domain binding motif, known to have the consensus
189 sequence of PPxY (Kasanov et al., 2001; Pirozzi et al., 1997), to fit our criterion. When
190 we mutated the PPDY motif of HA-NL2-RM to four alanines, we found that this construct
191 could not rescue the astrocyte complexity (Fig 2H-J). Similarly, mutation of the PPDY
192 (PPDY > AAAA) in the NL2 ECD/NL1 ICD chimera ablated the morphogenesis rescue
193 previously seen for the non-mutated chimera (Fig 2H-J). Together, these data suggest
194 that NL2 controls astrocyte morphogenesis through PPDY motif interactions in its ICD.

195 ***In vivo* BioID reveals unique interactions of astrocytic Neuroligins, including WW**
196 **domain-containing proteins**

197 PPxY motifs are recognized by Group I WW domain-containing proteins (Kato et al.,
198 2004, 2002). WW domains are ~40 amino acids, with two flanking conserved tryptophan
199 (single amino acid code: W) residues (Sudol and Hunter, 2000). In the human

200 proteome, there are over 50 proteins that contain a WW domain, with many containing
201 multiple WW domains. To identify which WW domain-containing protein binds NL1 and
202 NL2, we used *in vivo* BioID (iBioID). This approach (Roux et al., 2012) uses a biotin
203 ligase, Turbo BirA, fused to a bait protein to identify all proteins interacting with the bait,
204 within 10nm (Branon et al., 2018). We made C-terminal fusions of Turbo BirA to NL1, 2,
205 or 3 and virally expressed these constructs under the control of the astrocyte promoter
206 GfaABC1D (Lee et al., 2008) (Fig 3A-D). To investigate cell-type specific differences in
207 the NL2 interactome, we also expressed NL2-Turbo BirA under the control of the
208 neuronal promoter hSyn1 (Fig 3A-B). As controls, we expressed soluble TurboID in
209 astrocytes or neurons, which will biotinylate the repertoire of intracellular proteins in
210 each cell-type. We chose to use a cytosol-localized control, as NLs are trafficked
211 throughout many cellular compartments (Kang et al., 2014; Binda et al., 2019; Halff et
212 al., 2019; Xie et al., 2023; Xu et al., 2024) , and we aimed to capture all physiologically
213 relevant interactors, not just those at the plasma membrane. We confirmed that the
214 NL2-Turbo BirA constructs were properly localized to the cell membrane in cultured
215 astrocytes (Fig S3A) and they could rescue the morphological deficits of shNL2
216 astrocytes (Fig S3B, C), thus indicating that NL2 functioned as expected. However, we
217 found that placing the Turbo BirA after the PDZ-binding motif in the NL2 ICD reduced
218 the enzyme's biotinylation activity. By moving the PDZ domain after the TurboID, we
219 observed robust biotinylation (Fig S3B) and proceeded with this placement of the
220 TurboID (before the PDZ binding motif) for all NL constructs (Fig 3A).

221 We injected perinatal mice (P0-P1) intracortically with AAVs expressing the NL-Turbo
222 BirA fusions, or the cell-type-specific soluble BirA control. After three days of biotin

223 injection (P18-P20), we collected P21 mouse cortices and isolated biotinylated proteins
224 by streptavidin immunoprecipitation (Figs 3A, E). We chose P21 as an endpoint
225 because NL2 loss in developing astrocytes results in significantly smaller astrocyte
226 territories with concomitant deficits in synapse formation and function at P21 (Stogsdill
227 et al., 2017). We confirmed the cell-type-specificity of biotinylation *in vivo* by co-staining
228 for the astrocytic marker Sox9 (Fig 3C-D) or the neuronal marker NeuN (Fig S3D). Mass
229 spectrometry identification and quantification of the biotinylated proteins (Fig S4 A-D,
230 Dataset S1) revealed substantial differences in the putative interactomes of astrocytic
231 NL1-3 (Fig 3F, Dataset S1), when normalized to their respective soluble TurboID
232 controls. Similarly, there were substantial differences between proteins proximal to
233 neuronal versus astrocytic NL2 (Fig 3F, Dataset S1).

234 We bioinformatically compared our data to previously published NL2 interactome data
235 (identified via NL2 co-immunoprecipitation in adult mouse whole brain (Kang et al.,
236 2014), *in vitro* extracellular NL2 APEX proximity proteomics (Loh et al., 2016), and a
237 yeast two-hybrid screen of the NL2 ICD (Poulopoulos et al., 2009)) and found a
238 significant overlap with our datasets for each of the previously published data (Fig 4A).
239 We also found noticeable differences between the astrocytic and neuronal interactome
240 of NL2. For example, neuronal NL2 is well characterized for interacting with the
241 inhibitory synapse scaffold protein, Gephyrin (Poulopoulos et al., 2009), which we
242 detected as highly enriched in the neuronal NL2 iBioID interactome (Fig 4B, Dataset
243 S1). However, even though Gepyhrin is present in astrocytes at both the mRNA (Zhang
244 et al., 2014) and protein levels (Dataset S1), we did not detect a significant enrichment
245 of Gepyhrin in the astrocytic NL2 iBioID (Fig 4B, Dataset S1). This result strongly

246 suggests cell-type-specific regulation of protein-protein interactions of NL2 and is
247 consistent with our finding that Gephyrin interaction with NL2 is not necessary for
248 astrocyte morphogenesis (Fig 2A, B).

249 Gene ontology analysis of the unique proximity interactomes across astrocytic NLs
250 suggests distinct functions of NLs in astrocytes (Fig 4C) and of astrocytic vs neuronal
251 NL2 (Fig 4D). These data support our earlier findings, showing that NLs have non-
252 redundant roles in astrocytes and that these differences likely extend beyond the control
253 of astrocyte morphogenesis. Further, gene ontology analysis of NL2-proximal proteins
254 in neurons and astrocytes reveals functional differences. Interestingly, only astrocytic
255 NL2 interacts with proteins that bind actin filaments (Fig 4D, S4E), which are abundant
256 in perisynaptic astrocyte processes (Soto et al., 2023). To facilitate further exploration
257 into the biological mechanisms governing NL control of astrocyte development and
258 function, we have compiled our dataset into a searchable website at https://eroglu-
259 neuroliginbioid.org/.

260 The putative NL2 interactome we identified enabled us to determine which nearby
261 proteins recognize the PPxY motif in NL2 and thus participate in NL2-dependent
262 astrocyte morphogenesis. To do so, we analyzed WW domain-containing proteins
263 across all datasets that were significantly enriched with the bait protein, compared to the
264 cytoplasmic control. Across the 4 iBioID experiments, we identified 9 WW-domain-
265 containing proteins in NL interactomes (Fig 4E). The WW domain-containing proteins
266 within the NL interactomes varied across NL isoforms and cell types. Even though NL1
267 and NL2 have identical PPxY motifs (PPDY, Fig 2G), there was minimal overlap in WW
268 domain-containing proteins that interacted with both. This finding suggests that the

269 interactions of NLs with WW domain-containing proteins *in vivo* are not solely
270 determined by the presence of the PPxY motif, and that additional protein-protein
271 interaction motifs in the ICD may confer specificity to these interactions. Furthermore,
272 the utility of including NL3 as a bait in our BioID experiments served as an informative
273 control for the PPxY motif, as NL3 contains the LPxY motif, which is only weakly bound
274 by WW proteins, providing a strong comparative reference for motif-dependent
275 interactions.

276 **The WW domain-containing E3 ubiquitin ligase Nedd4l is necessary for astrocyte**
277 **morphogenesis, but not synaptogenesis**

278 The binding of WW domains to WW motifs has various physiological effects in the cell,
279 including cellular growth (Lee et al., 2020), endocytosis of membrane proteins (Totland
280 et al., 2017), and transcription (Sudol et al., 2001). Importantly, WW domain-containing
281 proteins and their interactions with WW motifs have been implicated in various
282 diseases, including the neurodevelopmental disorder Rett Syndrome (Rodrigues et al.,
283 2020), Muscular Dystrophy (Ilsley et al., 2002), and hypertension (Minegishi et al.,
284 2016). We observed three significantly enriched WW domain-containing protein
285 interactors of astrocytic NL2, Dystrophin (*Dmd*), growth arrest-specific protein 7 (*Gas7*),
286 and neural precursor cell expressed developmentally downregulated 4-like protein
287 (*Nedd4l*, also called Nedd4-2) (Fig 4E). We chose to focus on Nedd4l for two reasons.
288 First, both NL1 and NL2 PPDY motifs are necessary for astrocyte morphogenesis (Fig
289 2I-J), and Nedd4l is enriched in astrocytic NL1 and NL2, but not NL3 (Fig 4E) proximity
290 proteomes. Second, Nedd4l has a known role in regulating astrocyte membrane
291 proteins. Nedd4l controls the abundance of the potassium channel Kir4.1, the gap

292 junction protein, Connexin-43 (Altas et al., 2024; Liu et al., 2021) as well as the
293 abundance and surface localization of the glutamate transporter Glt-1 (Zhang et al.,
294 2017), via ubiquitination.

295 To investigate if Nedd4l is necessary for astrocyte morphogenesis, we designed and
296 validated an shRNA (Figs 5A, S5A-B) targeting *Nedd4l*, and expressed it in astrocytes
297 cultured with wild-type neurons. We observed a striking reduction in astrocyte
298 morphological complexity in shNedd4l-transfected astrocytes, compared to control (Fig
299 5A-B). Co-knockdown of *Nedd4l* and *Nlgn2* (using a plasmid that also encodes
300 mCherry) did not further reduce astrocyte complexity. These findings suggest that
301 Nedd4l and NL2 might work in the same pathway (Fig 5B).

302 Next, we tested whether Nedd4l is necessary for astrocyte morphogenesis *in vivo*. To
303 achieve genetically targeted and sparsely labeled astrocytes in the mouse cortex, we
304 used postnatal astrocyte labeling by electroporation (PALE) (Baldwin et al., 2021;
305 Stogsdill et al., 2017). In this method, plasmid DNA expressing a shRNA with
306 CAG:mCherry-CAAX and a GLAST promoter-driven piggyBac enzyme are injected into
307 P0-P1 mouse lateral ventricles and then electroporated into the cortex. This technique
308 results in the uptake of the plasmid by radial glia and subsequent astrocyte labeling
309 after differentiation (Fig 5C). We previously found that reducing astrocytic NL2 by PALE,
310 either by using an shRNA or a floxed allele for *Nlgn2* with astrocytic Cre expression,
311 results in a significantly stunted astrocyte territory volume and branch complexity
312 (Stogsdill et al., 2017). We used confocal imaging of the entire astrocyte in 100μm
313 tissue sections and reconstructed the astrocyte volume using Imaris software.
314 Quantification of the astrocyte territory volume revealed a significant reduction in

315 shNedd4l astrocytes, compared to a scrambled shRNA control (shCtrl) (Fig 5D-E).
316 Additionally, quantification of the astrocyte complexity using *in vivo* Sholl analysis
317 revealed a significant decrease in complexity of Nedd4l knockdown astrocytes (Fig 5F).
318 These data suggest that astrocyte morphogenesis is controlled by Nedd4l at both the
319 level of territory size and branch complexity.

320 We previously showed that loss of *Nlgn2* in single astrocytes in the mouse V1 cortex
321 also results in reduced excitatory synaptogenesis in the surrounding neuropil. Thus, to
322 test if Nedd4l loss also affects synapse density, we used PALE to knock down *Nedd4l* in
323 sparse astrocytes in the mouse V1 cortex. At P21, we stained cortical sections for
324 presynaptic Bassoon, and postsynaptic PSD95 and Gephyrin. With this strategy, we
325 quantified both excitatory (closely apposed Bassoon and PSD95) and inhibitory
326 (Bassoon and Gephyrin) synapses in the same sections (Fig S5C). We used the
327 mCherry signal from the piggyBAC vector (Fig 5C) to define astrocyte territories. Using
328 open-source SynBot software (Savage et al., 2024), we quantified the synaptic density
329 within and outside of labeled astrocytes (Fig S5C-D). These data revealed no significant
330 differences in synapse density in *Nedd4l*-knockdown astrocytes, *in vivo* (Fig S5E-F).
331 This data suggests Nedd4l and its interaction with NL2 controls astrocyte morphological
332 development independently from the role of astrocytic NL2 in synaptogenesis, and
333 Nedd4l does not have an independent role in astrocyte-dependent synaptogenesis.

334 **The PPDY motif in Neuroligin-2 is sufficient for Nedd4l interaction**

335 Nedd4 proteins exhibit preferential binding to PPxY motifs and only weakly bind to LPxY
336 (Hatstat et al., 2021). In the absence of a PPxY containing substrate, Nedd4l is known
337 to bind its own LPxY motif, autoubiquitinate and degrade (Bruce et al., 2008). Because

338 NL1 and NL2 have a PPxY motif, and NL3 has an LPxY motif (Fig 2G; Fig S2B), we
339 wondered if Nedd4l preferentially and directly interacted with NL1 and NL2 ICDs but not
340 the NL3 ICD. To test this, we used either the wildtype NL2 or NL2 ECD/NL1 ICD
341 chimera (Fig 2D) or the mutated PPDY motif constructs that abolish the WW domain-
342 containing motif, as described earlier (Fig 2H-J; Fig 6A). Conversely, we also mutated
343 the NL3 ICD LPDY motif to PPDY to mimic NL1 and NL2 ICDs. All chimeric constructs
344 contained the NL2 ECD to rule out the effects of sequence divergence in NL ECDs.

345 Next, we co-expressed HA-tagged NL2 or NL2 chimeras with V5-tagged Nedd4l in HEK
346 293T cells and co-immunoprecipitated NLs using anti-HA tag magnetic beads. We
347 found that Nedd4l co-immunoprecipitated with wildtype NL2 (Fig 6B); however, ablation
348 of the PPDY motif in NL2 ICD (NL2ΔWW, Fig 6A) resulted in a substantial, yet variable,
349 reduction of Nedd4l co-immunoprecipitation (Fig 6B, C). A previous study investigating
350 the interaction of NL2 and the WW domain-containing protein S-SCAM (*Magi2*) found
351 that a longer stretch of amino acids (766-796), which contains the PPDY motif, in the
352 NL2 ICD is necessary for direct binding of S-SCAM to NL2 (Sumita et al., 2007). Thus,
353 we next deleted these amino acids from the NL2 ICD (NL2ΔWWLrg, Fig 6A) and
354 performed co-immunoprecipitation with Nedd4l. Loss of this sequence in NL2 ICD
355 completely abolished the interaction with Nedd4l (Fig 6D-E), demonstrating that this is a
356 critical region in NL2 ICD containing the PPDY motif that mediates Nedd4l binding.

357 Ablation of the PPDY motif in NL1 ICD (NL2/1ΔWW, Fig 6A), however, abolished the
358 interaction with Nedd4l entirely, further showing the importance of the PPDY motif in
359 NL-Nedd4l interactions (Fig 6F-G). As expected, we found that Nedd4l does not interact
360 with wild-type NL3 ICD (Fig 6H). However, mutating the LPDY motif of NL3 ICD to

361 PPDY (NL2/3WW, Fig 6A, H-I) was sufficient to induce an interaction between Nedd4l
362 and NL3 ICD. These results reveal that the PPDY is sufficient for Nedd4l interactions
363 with NL ICDs. Additional sequences in the NL2 ICD between amino acids 766-796
364 flanking the PPDY motif are also involved in NL2/Nedd4l binding.

365 **Nedd4l ubiquitinates Neuroligin-2 at K749, resulting in increased stability of**
366 **Neuroligin-2**

367 Nedd4l is an E3 ubiquitin ligase of the HECT domain family, which has previously been
368 shown to polyubiquitinate the astrocyte membrane proteins Kir4.1, Connexin-43, and
369 Glt-1, resulting in their degradation (Altas et al., 2024; Liu et al., 2021; Zhang et al.,
370 2017). Previous proteomic studies have identified that the intracellular domain of NL2 is
371 ubiquitinated at lysine 749 (K749) (Na et al., 2012; Wagner et al., 2012) in both mouse
372 and rat brain tissues. However, the function of this post-translational modification in NL2
373 is unknown. Thus, we investigated whether NL2 is ubiquitinated at K749. To do so, we
374 first blocked proteasomal degradation using the proteasomal inhibitor MG-132. We next
375 heat-denatured lysates to disrupt protein-protein interactions and subsequently
376 immunoprecipitated HA-NL2 from primary rat astrocytes. After running the
377 immunoprecipitated eluates on a western blot, we found that HA-NL2 showed a smear
378 of high molecular weight HA-immunoreactive protein, indicative of polyubiquitinated
379 protein (Fig 7A). We found that we could significantly decrease this smear by mutating
380 K749 to R (Arginine), as immunoprecipitation of HA-NL2K749R only showed one
381 predominant band at the molecular weight of NL2, indicating this smear is likely
382 ubiquitination (Fig 7A-B).

383 We next aimed to test if Nedd4l ubiquitinates NL2. Interestingly, while the *Nedd4l*
384 expression construct works well in HEK 293T cells, we were unable to overexpress
385 Nedd4l in primary astrocytes. This may be caused by global proteasome disruptions
386 and cytotoxicity due to Nedd4l's role in astrocyte protein turnover (Altas et al., 2024).
387 Therefore, we used HEK 293T cells to express HA-NL2 with or without V5-Nedd4l and
388 probed for GFP-tagged ubiquitination by western blot using a GFP antibody. We found
389 that, compared to NL2 alone, co-expression with Nedd4l resulted in a high-molecular-
390 weight smear above the expected NL2 size, indicating that Nedd4l is sufficient to
391 enhance polyubiquitination of NL2 (Fig S5G-H). Further, we could reduce ubiquitination
392 by mutating NL2 K749 to arginine (K749R). Co-expression of Nedd4l and NL2K749R
393 did not result in strongly enhanced polyubiquitination of NL2, indicating that K749 is the
394 major ubiquitination residue in NL2, but others may be present (Fig S5G-H). Together,
395 these data reveal that Nedd4l is sufficient to ubiquitinate NL2 at K749.

396 While ubiquitination is typically associated with protein degradation, it can also serve as
397 a post-translational signal for various cellular processes (Mukhopadhyay and Riezman,
398 2007). We first tested whether Nedd4l-mediated ubiquitination of NL2 leads to its
399 degradation. We expressed NL2 with or without Nedd4l in HEK cells and collected cell
400 lysates at different time points after cycloheximide (CHX) treatment, which blocks
401 nascent translation. Western blotting of these samples revealed a decrease in HA-NL2
402 abundance over time, indicating NL2 is degraded (Fig 7C-D). Strikingly, co-expression
403 of Nedd4l with NL2 completely blocked this degradation and stabilized the NL2 protein
404 over time (Fig 7C-D). Interestingly, the NL2K749R ubiquitination mutant was sufficient
405 to block NL2 degradation, with no further effect by the addition of Nedd4l (Fig 7E-F).

406 Taken together, these data reveal that ubiquitination at K749 controls NL2 degradation;
407 however, ubiquitination at K749 by Nedd4l stabilizes the NL2 protein and prevents its
408 degradation.

409 **Ubiquitination of Neuroligin-2 at Lysine 749 is required for astrocyte**
410 **morphogenesis**

411 NL2 is ubiquitinated *in vivo* (Na et al., 2012; Wagner et al., 2012), yet whether
412 ubiquitination at this residue has a functional role is unexplored. Therefore, we next
413 tested if ubiquitination at K749 is necessary for NL2's control of astrocyte
414 morphogenesis. To do so, we expressed NL2K749R (also mutated to be resistant to
415 shNL2) in primary astrocytes and subsequently co-cultured the astrocytes on top of
416 neurons to quantify astrocyte complexity. Surprisingly, we found that NL2K749R
417 expression significantly reduced astrocyte morphology in a dominant-negative fashion
418 compared to the shRNA control (Fig 8A-B). NL2K749R was incapable of any
419 morphological rescue of shNL2-transfected astrocytes (Fig 8A-B).

420 Finally, we investigated whether NL2K749R is crucial for astrocyte morphogenesis in
421 the developing mouse cortex. In *Nlgn2* homozygous flox animals (*Nlgn2* $^{fl/fl}$), also
422 carrying a Rosa26:lox-STOP-lox tdTomato allele, we used PALE (Fig 5C) to express
423 Cre to ablate *Nlgn2* in astrocytes, while simultaneously expressing HA-NL2 (WT) or HA-
424 NL2K749R (Fig 8C). At P21, we harvested the brains to analyze astrocyte
425 morphological development via Imaris reconstruction and 3D Sholl analysis. As
426 previously shown (Stogsdill et al., 2017), the knock-out of both copies of *Nlgn2* via Cre
427 expression in astrocytes results in a significantly diminished territory volume, compared
428 to *Nlgn2* $^{+/+}$ animals (also carrying the Rosa26:lox-STOP-lox tdTomato allele) (Fig 8D).

429 This morphological deficit was rescued by co-expressing an HA-tagged NL2 plasmid in
430 the astrocytes (Fig 8D). Supporting our *in vitro* findings (Fig 8B), co-expression of HA-
431 NL2K749R with Cre in *Nlgn2* $^{fl/fl}$ astrocytes was not able to rescue the reduction in
432 territory volume and showed no significant difference from *Nlgn2* $^{fl/fl}$ astrocytes that
433 received only Cre (Fig 8D). We observed a bimodal distribution in the territory volumes
434 of *Nlgn2* $^{fl/fl}$ astrocytes that received Cre + HA-NL2K749R, which was not related to sex
435 or astrocyte layer identity, suggesting that an unknown variable influences the functional
436 importance of NL2 ubiquitination status.

437 Using 3D Sholl analysis (Fig. 8E), we observed a trend toward increased branch
438 complexity in HA-NL2–expressing astrocytes compared to Nlgn2 $^{fl/fl}$ astrocytes
439 expressing Cre alone; however, this difference did not reach statistical significance. In
440 contrast, astrocytes expressing HA-NL2K749R showed no improvement in branch
441 complexity relative to *Nlgn2*-deficient astrocytes. We next calculated the total number of
442 intersections as a summary measure of astrocyte complexity (Fig. 8F). This analysis
443 revealed that *Nlgn2* deletion significantly reduces total branch complexity, which is
444 restored by HA-NL2 but not HA-NL2K749R expression. Notably, HA-NL2K749R-
445 expressing wildtype astrocytes also remained significantly less complex than both wild-
446 type controls and HA-NL2 rescue astrocytes.

447 Together with the robust rescue of territory volume (Fig. 8D), these findings
448 demonstrate that wild-type NL2 restores astrocyte morphogenesis, but ubiquitination-
449 deficient NL2K749R mutant fails to do so. These results support a model in which
450 Nedd4L-mediated ubiquitination of NL2 is required for its proper function in regulating
451 astrocyte morphogenesis *in vivo*.

452 **DISCUSSION**

453 Astrocytes play crucial roles in nervous system development and function. These
454 functions rely on astrocytes' highly branched morphology, which is largely controlled by
455 cell-adhesion molecules (Ackerman et al., 2021; Baldwin et al., 2021; Stogsdill et al.,
456 2017; Tan et al., 2023). However, the mechanisms downstream of these cell adhesion
457 molecules are not fully understood. Here, we show that NLs are non-redundant in
458 controlling astrocyte morphology due to their unique intracellular protein interactomes.
459 We found a critical motif that regulates Nedd4l interaction and ubiquitination of NL2,
460 which is necessary for NL2-mediated control of astrocyte morphogenesis. Further, we
461 provide *in vivo* astrocytic NL1-3 and neuronal NL2 proximity proteomes, which provide
462 insights into the differences in astrocytic NL function and cell-type-specific functions of
463 NL2 between astrocytes and neurons.

464 How do NLs uniquely contribute to astrocyte morphogenesis? We found that
465 overexpression of NLs could not compensate for the loss of one another *in vitro*, which
466 may be due to several factors. First, NL mRNA expression patterns differ in the
467 developing cortex (Clarke et al., 2018), suggesting that temporal dynamics of NLs may
468 differentially control astrocyte cytoarchitecture. Second, NLs form both homo- and
469 heterodimers, and dimerization is necessary for both localization and function
470 (Poulopoulos et al., 2012; Shipman and Nicoll, 2012). In neurons, only NL1/NL3 and
471 NL1/NL2 heterodimers have been detected (Poulopoulos et al., 2012); however, our
472 results indicate that both NL1/NL2 and NL2/NL3 heterodimers are present in both
473 astrocytes and neurons, suggesting that cell-type-specific heterodimers may impact NL
474 function during brain development. Lastly, our interactome data reveal distinct protein

475 interactions of NLs, which likely contribute to unique astrocytic NL function.
476 Interestingly, gene ontology analysis revealed a significant interaction with actin-binding
477 proteins and cytoskeletal-related proteins specifically in astrocyte NL2, and minimally in
478 astrocyte NL1, NL3, or neuronal NL2, suggesting that astrocytic NL2 plays a dominant
479 role in controlling cell morphology (Dataset S2, Fig S4 E-F). It is important to note a few
480 limitations of our iBioID data: first, because the TurboID promiscuously biotinylates
481 proteins within 10nm, interactions with a bait protein (here, NLs) may or may not be due
482 to direct binding and should be validated orthogonally, as we showed with Nedd4l (Fig
483 6). Second, interactions with NLs may be transient and/or developmentally regulated,
484 and thus, our 3-day biotinylation treatment window may capture both static and transient
485 interactions. Therefore, these data should not be interpreted as a compendium of NL-
486 interacting proteins. Lastly, GFAP promoter activity is highest in the lower layers of the
487 cortex (Fig 3C-D), thus our astrocyte-specific proteomic experiments are largely
488 influenced by lower-layer astrocytes. Nevertheless, the iBioID interactomes generated
489 in this study will be beneficial in elucidating the mechanisms through which NLs control
490 astrocyte structure and function.

491 In this work, we show that the WW domain-containing protein Nedd4l is critical for
492 astrocyte morphogenesis, and this protein has distinct specificity for each NL, which we
493 validated by coimmunoprecipitation. How do WW domain proteins specify interactions
494 with NLs? Nedd4l preferentially binds PPxY motifs, but can also weakly bind LPxY
495 (Bruce et al., 2008; Hatstat et al., 2021). We identified that NL1 and NL2 contain a
496 PPxY motif in their ICDs, whereas NL3 contains an LPxY motif. This single amino acid
497 change ultimately affects Nedd4l's binding to NLs but does not fully explain the

interaction specificity. Only after deleting amino acids 766-796 in NL2 is Nedd4l binding blocked, suggesting a larger surface is critical for the interaction between NL2 and Nedd4l. This may explain why mutation of PPDY to AAAA in the NL2 ICD still restores some astrocyte complexity (Fig 2J) and suggests that the WW-binding motif in NL2 is not the sole determinant of NL2 function in astrocyte morphogenesis. Moreover, in our iBioID results, Nedd4l is not enriched in the NL1 proximal proteome as strongly as NL2 in astrocytes, which may indicate a weaker physiological interaction. Tyrosine phosphorylation in WW motifs is known to occlude binding with WW domains (Chen et al., 1997). The conserved Tyrosine (Y) in the PPxY motif is the same residue that modulates Gephyrin binding (Y770) (Poulopoulos et al., 2009) and is phosphorylated in neuronal NL1 but not neuronal NL2 (Letellier et al., 2018), therefore, phosphorylation and/or Gephyrin binding may modulate Nedd4l binding to NLs. Nedd4l interactions with its known targets are controlled through adapter proteins, namely the 14-3-3 family (Lee et al., 2018; Nagaki et al., 2006). Our data reveal that astrocytic NL2 interacts with several members of the 14-3-3 family, which may influence Nedd4l-NL interactions in astrocytes. Lastly, several WW domain-containing proteins interact with NLs in a cell-type-specific manner (Fig. 4E). Future studies will reveal the cell-type-specific effects of WW domain-containing protein interactions with NLs.

Until this study, the functional consequence of NL2 ubiquitination had not been demonstrated in either astrocytes or neurons. We found that Nedd4l ubiquitinates NL2 at K749. Numerous reports have shown that Nedd4l ubiquitinates the astrocytic targets Kir4.1 and Connexin-43 (Altas et al., 2024), resulting in proteasome-mediated degradation (Liu et al., 2021; Zhang et al., 2017; Zhou et al., 2007). However, here we

521 found that Nedd4l ubiquitination of NL2 stabilizes NL2. Interestingly, ubiquitination-
522 mediated protein stabilization has been reported previously for other HECT E3 ubiquitin
523 ligases (Xu et al., 2015). We speculate that Nedd4l-mediated NL2 stability may maintain
524 the surface pool of NL2 and/or overall NL2 abundance, thereby supporting synaptic
525 contacts with Neurexins.

526 While Nedd4l ubiquitination of NL2 does not lead to protein degradation, our data reveal
527 that NL2K749 ubiquitination can be a degradative signal. In HEK cells, NL2 protein
528 abundance significantly decreases over time, and blocking ubiquitination at K749
529 prevents this degradation (Fig 7C-F). The functional consequences of ubiquitination at
530 NL2 may differ based on the E3 ubiquitin ligase that targets NL2 and/or the subcellular
531 localization of the ubiquitination event. It is possible that NL2 is ubiquitinated by Nedd4l
532 at the cell membrane, where Nedd4l is localized, leading to NL2 stabilization. If Nedd4l
533 cannot ubiquitinate NL2, NL2 may be internalized and targeted for degradation by
534 another E3 ubiquitin ligase. It will be important to disentangle the type of ubiquitin chain
535 attached to NL2 in the presence or absence of Nedd4l.

536 A limitation of this experiment is that it was performed in heterologous cells, due to the
537 low expression of astrocytic NL2 in the absence of neurons, possibly resulting from
538 rapid degradation. Future work using cell-type-specific knock-in or conditional
539 degradation models will be required to test Nedd4l's role in regulating NL2 stability in
540 astrocytes, *in vivo*. However, we did detect a high-molecular-weight smear in HA-NL2 in
541 primary rat astrocytes, which is sharply diminished in HA-NL2K749R-expressing cells,
542 highly suggestive of poly-ubiquitination. The identity of this smear can be resolved in the
543 future using direct assays of polyubiquitination, including chain-specific

544 polyubiquitination events. Lastly, these findings also provide insight into how
545 perturbations in NL2 abundance disrupt astrocyte morphology. We find that the
546 NL2K749R mutation (Fig 8A-B), which may stabilize the NL2 protein in astrocytes by
547 preventing proteasome-mediated degradation, acts in a dominant-negative manner (Fig
548 7C-D). Interestingly, we do not observe an effect on astrocyte morphology with
549 overexpression of wild-type NL2 (Fig S1C, D), suggesting that excessive NL2 in
550 astrocytes is not sufficient to explain the dominant-negative effect of NL2K749R. Our
551 findings suggest that the balance between NL2 stabilization and degradation is
552 controlled by ubiquitination of K749. We postulate that this modification is crucial for
553 regulating NL2 levels and surface localization to establish proper neuron-astrocyte
554 adhesions and support astrocyte morphogenesis.

555 Finally, proteomics data revealed that NL2 is ubiquitinated at lysine K749 in both mouse
556 and rat brains, whereas NL1 and NL3 are not (Na et al., 2012; Wagner et al., 2012). We
557 found that blocking ubiquitination at K749 results in a stunted morphological phenotype
558 for NL2-mediated astrocyte morphogenesis, both *in vitro* and *in vivo* (Fig 8A-F). This
559 phenotype may be due to mislocalized NL2, thus leading to improper targeting of
560 perisynaptic astrocyte processes in the neuropil and preventing precise interactions with
561 neuronal neurexins. To this end, understanding how trans-synaptic neurexin binding to
562 NL2 affects Nedd4l interaction with NL2 and/or NL2 ubiquitination is an important future
563 direction. Altogether, this finding underscores the importance of NL2 turnover in the
564 development of astrocyte morphology.

565 Emerging evidence emphasizes the differential roles of astrocytic versus neuronal NLs.
566 Numerous laboratories have identified physiological roles of NLs in various glia

567 including astrocytes (Stogsdill et al., 2017; Ackerman et al., 2021), oligodendrocyte
568 precursor cells (Li et al., 2024), as well as glioma (Venkatesh et al., 2015, 2017).
569 Recently, a study claimed that astrocytic NLs do not control astrocyte morphogenesis or
570 synapse formation (Golf et al., 2025). Using a tamoxifen-inducible astrocyte Cre line
571 and floxed NL alleles to knock out *Nlgns1-3* in the mouse brain, the authors
572 demonstrate a decrease in astrocyte-specific ribosome-bound NL mRNA only at 8
573 weeks postnatally but show no difference in cortical astrocyte morphology at P35. We
574 suspect that their incongruous findings are due to incomplete knockdown of NLs early in
575 development, which we have shown to be particularly difficult to knock out *in vivo* using
576 the traditional Cre-Lox system (Stogsdill et al., 2017). In this work, to circumvent such
577 issues, we have used carefully validated shRNAs (Chih et al., 2006) *in vitro* and *in vivo*,
578 which have no compounding effect in NL2 cKO astrocytes, indicating no off-target
579 effects (Stogsdill et al., 2017), and we have validated these findings using the CRISPR-
580 Cas9 system (Fig S1E-H) and PALE-mediated KO and rescue of NL2-dependent
581 astrocyte morphogenesis (Fig 8C-F).

582 In summary, we provide new insights into NL-mediated control of astrocyte
583 morphogenesis and reveal that the WW domain-containing protein Nedd4l is required
584 for astrocyte morphogenesis by ubiquitinating and stabilizing NL2. Lastly, we show that
585 NL2 ubiquitination is critical for astrocyte morphogenesis, *in vitro and in vivo*.

586 **Acknowledgments**

587 This work was supported by the National Institutes of Health (R01 NS102237; R01
588 DA047258 to C. Eroglu, F32 NS112565 to K. Sakers, and F31NS125985 to J.J.

589 Ramirez), and fellowships from The Ruth K. Broad Biomedical Research Foundation (N.
590 Elazar) and the Life Sciences Research Foundation (N. Elazar).

591 We thank Dr. Roger Nicoll for the NL chimeric constructs. We thank members of Dr.
592 Scott Soderling's lab for iBioID constructs and protocols. We thank Dr. Dolores Irala for
593 her help with figure organization. We thank Dr. Jessica Moore, Dr. Dolores Irala, Dr. Jeff
594 Stogsdill and Dr. Debra Silver for critical review of this manuscript. C. Eroglu is an HHMI
595 Investigator.

596

597 **MATERIALS & METHODS**

598 **Mice**

599 All mice and rats were used in accordance with the Institutional Animal Care and Use
600 Committee (IACUC), under the guidance of the Duke Division of Laboratory Animal
601 Resources (DLAR) with protocol numbers A147-17-06, A117-20-05, and A103-23-04.
602 All animals were housed in 12-hour light/dark cycles. Timed-pregnant CD1 female mice
603 (RRID: IMSR_CRL:022) were used for PALE and iBioID experiments, obtained from
604 Charles River Laboratories. The NL2 floxed (B6;SJL-Nlgn2tm1.1Sud/J; Stock #025544,
605 RRID:IMSR_JAX:025544), and Ai14 (RTM) (B6;129S6-Gt(ROSA)26Sortm14(CAG-
606 tdTomato)Hze/J; Stock #007908, RRID:IMSR_JAX:007908) animals were obtained
607 through Jackson Laboratory. CD Sprague-Dawley IGS Rats (SD-001, RRID:
608 IMSR_CRL:400) were used for primary culture preps, obtained from Charles River
609 Laboratories. Mice and rats of both sexes were pooled and included in all experiments.

610 **Plasmids:**

611 *shRNA plasmids:*

612 shRNAs for NL1(RRID:Addgene_59339), 2 (RRID:Addgene_59358), and 3
613 (RRID:Addgene_59359) and scrambled NL shRNA control (shCtrl) constructs were
614 described previously(Stogsdill et al., 2017). Antisense shRNA sequences:
615 Nlgn1: CCCAACACTATACCAGGGATT
616 Nlgn2: GGAGCAAGTTCAACAGCAA
617 Nlgn3: GCCCTTGGACTTAACATTTAT

618 shRNAs were cloned into pLKO.1 vector (a kind gift from David Root, Addgene plasmid
619 #10878, RRID: Addgene_10878). A CAG-eGFP sequence was introduced into the
620 vector for expression in primary astrocytes. Antisense shRNA sequences:

621 - Nedd4l: TTTATTAAGGGCTTTGCCTGC (Horizon Discovery, TRCN0000086868)

622 For PALE, the same shRNA sequence was cloned into a piggyBAC transposon system
623 expressing mCherry CAAX and transfected with a GLAST-piggyBACase plasmid (a kind
624 gift from Dr. Joseph LoTurco) as previously described(Tan et al., 2023). The Nedd4l
625 shRNA in the piggybac backbone is available at Addgene (RRID:Addgene_249589).

626 *NL chimeric plasmids:*

627 Chimeric HA-NL2 constructs were a kind gift from Dr. Roger Nicoll and described
628 previously(Nguyen et al., 2016) (NL2/1 Chimera RRID_Addgene_249601; NL2/3
629 Chimera RRID_249602). These constructs were modified to be resistant to
630 shNL2(Stogsdill et al., 2017).

631 *HA-NL2 mutation plasmids:*

632 All plasmids below were made in the HA-NL2-RM backbone, to be resistant to shNL2.

633 Deletion of the PDZ domain (RRID:Addgene_249594), poly-proline domain
634 (RRID:Addgene_249595), and mutation of WW domains (PPDY → AAAA in NL2
635 (RRID:Addgene_249600), Large WW Deletion (a.a. 766-796 deletion,
636 RRID:Addgene_249599), PPDY → AAAA in NL1/2 chimera (RRID:Addgene_249597)
637 or LPDY → PPDY in NL3 chimera (RRID:Addgene_249598)) and K749R
638 (RRID:Addgene_249588) were performed using custom gene blocks (IDT) in the HA-

639 NL2-RM backbone. Mutation of the gephyrin binding residue in HA-NL2-RM (HA-NL2-
640 GBM-RM RRID:Addgene_249596) was performed via site-directed mutagenesis using
641 the QuikChange Lightning kit (Agilent) and the following primers:

642 Sense: 5' GCGCCCTGCCTGTgcagccGACgctACCCTGGCCTTGCGCCG 3'

643 Antisense: 5' GCCCGGCGCAAGGCCAGGGTAGCGTCggctgcACAGGCAG 3'.

644 *TurboID plasmids:*

645 pZac2.1-gfaABC1D-Turbo-BirA plasmid was a kind gift from Dr. Scott Soderling. The
646 NL-Turbo fusion constructs were made by PCR amplification from the HA-tagged
647 expression plasmids and subsequent In-Fusion cloning (Takara). A flexible glycine
648 hexamer linker was inserted between the NL expression sequence and the Turbo-BirA.
649 pZac2.1-GFABC1D-Turbo-BirA was digested with XhoI and NotI to release the Turbo-
650 BirA to insert HA-NL1/2/3-Turbo-BirA. The gfaABC1D promoter was swapped for hSyn1
651 for neuronal expression of NL2-TurboID. The TurboID constructs are available through
652 Addgene: gfaABC1D HA-NL2 Turbo RRID:Addgene_249590; gfaABC1D HA-NL1 Turbo
653 RRID:Addgene_249591; gfaABC1D HA-NL3 Turbo RRID:Addgene_249592; hSyn1 HA-
654 NL2 Turbo RRID:Addgene_249593.

655 *Expression plasmids:*

656 HA-NL1 (RRID:Addgene_15227), HA-NL2 (RRID:Addgene_15259) and HA-NL3
657 (RRID:Addgene_59318) were previously described(Stogsdill et al., 2017). V5-Nedd4l
658 was made by custom geneblock cloning (IDT) from the HA-Nedd4l (human sequence, a
659 kind gift from Joan Massague (Addgene plasmid # 27000; RRID:Addgene 27000)).
660 GFP-Ubiquitin was a kind gift from Nico Dantuma (Addgene plasmid # 11928;

661 RRID:Addgene 11928). For NL2 rescue PALE experiments, the CMV promoter was
662 replaced with GfaABC1D(Lee et al., 2008) for both HA-NL2 (RRID:Addgene_249587) or
663 HA-NL2K749R (RRID:Addgene_249588) via In Fusion Snap Assembly (Takara).
664 pCAG-Cre was a gift from Connie Cepko (Addgene plasmid # 13775 ;
665 http://n2t.net/addgene:13775 ; RRID:Addgene_13775).

666 *CRISPR plasmids:*

667 pX601-mCherry was a gift from Yuet Wai Kan (Addgene plasmid # 84039 ;
668 http://n2t.net/addgene:84039 ; RRID:Addgene_84039). The CMV promoter was
669 replaced with GfaABC1D promoter from the Turbo-BirA plasmids. SaCas9 gRNAs
670 targeting rat *Nlgn2* were designed using CRISPOR(Concordet and Haeussler, 2018)
671 software, and cloned into the BsaI sites in the pX601 vector.

672 - *Nlgn2* gRNA1: AAGAACTGCACGACCGGGCC
673 - *Nlgn2* gRNA2: GTGGTGAACACAGCCTACGG (RRID:Addgene_250933)
674 - *Nlgn2* gRNA3: GCCACACTCAACTACCGTCT (RRID:Addgene_250934)

675 For the CRISPR GFP translation assay, we cloned the NL2 gRNAs and their PAM
676 sequences upstream of and in frame with GFP under the control of the chicken beta
677 actin promoter.

678 **Rat astrocyte and neuron co-culture:**

679 Astrocyte and neuron cultures were performed as described(Baldwin et al., 2021;
680 Stogsdill et al., 2017). Briefly, P1 rat cortices were dissected and digested in ~7.5
681 units/ml Papain (Worthington). A single-cell suspension was extracted by gentle
682 pipetting with ovomucoid solutions (Worthington). Cells were filtered through a 20μm

683 mesh membrane (Elko Filtering 03-20/14) and then split for astrocyte and neuron
684 cultures.

685 For neuronal isolation, cortical cells were applied to negative panning dishes coated
686 with Bandeiraea Simplicifolia Lectin 1 (x2), followed by AffiniPure goat anti-mouse
687 IgG+IgM (H+L) (Jackson ImmunoResearch 115-005-044, RRID: AB_2338451), and
688 AffiniPure goat anti-rat IgG+IgM (H+L) (Jackson ImmunoResearch 112-005-044,
689 RRID:AB_2338094) antibodies to bind unwanted cells and debris. Cell suspensions
690 were passed onto positive panning dishes coated with mouse anti-L1 (ASCS4,
691 Developmental Studies Hybridoma Bank, Univ. Iowa, RRID:AB_528349) to bind cortical
692 neurons (>95% neuron). Adherent cells were collected following several washes with
693 DPBS (Gibco 14287) (supplemented with BSA and insulin) and forceful pipetting with a
694 P1000 pipette. Isolated neurons were pelleted (11 minutes at 200 g) and resuspended
695 in serum-free neuron growth media (NGM; Neurobasal, B27 supplement, 2 mM L-
696 Glutamine, 100 U/mL Pen/Strep, 1 mM NaPyruvate, 4.2 µg/mL Forskolin, 50 ng/mL,
697 BDNF, and 10 ng/mL CNTF). 100,000 neurons were plated onto 12 mm glass
698 coverslips (24-well plate) coated with 10 µg/mL poly-D-lysine (PDL, Sigma P6407) and
699 2 µg/mL laminin, and incubated at 37oC in 10% CO2. On DIV2, neurons were treated
700 with 10µM AraC for one day. Further, on DIV2, media was changed to Neurobasal Plus
701 Growth Media (NGM+; Neurobasal Plus, B27 Plus supplement, 100 U/mL Pen/Strep, 1
702 mM NaPyruvate, 4.2 µg/mL Forskolin, 50 ng/mL, BDNF, and 10 ng/mL CNTF). Neurons
703 were given a 50% media change every third day until astrocyte co-culture. A detailed
704 protocol can be found at: https://www.protocols.io/view/glia-free-cortical-neuron-culture-
705 36wgq3r35lk5/v1.

706 For astrocyte cultures, cortical cells were centrifuged and resuspended in astrocyte
707 growth medium (AGM; DMEM (Gibco 11960), 10% FBS, 10 µM, hydrocortisone, 100
708 U/mL Pen/Strep, 2 mM L-Glutamine, 5 µg/ml Insulin, 1 mM NaPyruvate, 5 µg/ml N-
709 Acetyl-L-cysteine). On the third day in vitro (DIV), astrocytes were washed with DPBS
710 and then shaken vigorously by hand until only adherent astrocytes remained. DPBS
711 was replaced with fresh AGM. AraC was added to the culture at DIV5 for two days. On
712 DIV7, astrocytes were passaged via Trypsin (Gibco) into 6- or 12-well dishes and then
713 transfected on DIV8 with Lipofectamine-LTX. On DIV10, transfected astrocytes were
714 trypsinized and resuspended into NGM+ and plated on neurons at a density of 20,000
715 cells per well (24 well plates). Cells were fixed after 48 hours of co-culture with warm
716 4% PFA (Electron Microscopy Sciences) for exactly 7 minutes.

717 **Immunocytochemistry:**

718 After fixation in 4% warmed PFA for 7 minutes (except in the case of surface staining in
719 which cold PFA was used for 5 minutes), coverslips were blocked in a blocking buffer
720 (150 NaCl, 50 Tris-base, 1% BSA, 100 mM L-lysine, 0.04% Sodium azide, pH 7.4)
721 containing 0.2% Triton X-100 (omitted in surface staining) and 50% NGS was added to
722 the coverslips for 30 minutes, followed by 2 washes of DPBS. Primary antibodies were
723 diluted in a blocking buffer containing 10% NGS and added to the coverslips overnight
724 at 4C. The following antibodies were used: GFAP (1:4000, rabbit, DAKO Z0334,
725 RRID:AB_10013382), GFP (1:1000, chicken, Millipore AB16901, RRID:AB_90890), HA
726 (1:1000, rat, Roche 11867423001, RRID:AB_390918), RFP (1:1000, rabbit, Rockland
727 600-401-379, RRID:AB_2209751). The next day, coverslips were washed 3 times with
728 PBS, and Alexa Fluor conjugated secondaries (Invitrogen: Rb 594, RRID:AB_2534079;

729 Ck 488 RRID:AB_2534096; Rat 594 RRID:AB_10561522) were diluted 1:1000 in
730 blocking buffer containing 10% NGS and incubated for 2 hours at room temperature.
731 After the incubation, the coverslips were washed 3 times and mounted onto glass slides
732 (VWR) with Vectashield mounting media containing DAPI (Vector Laboratories).
733 Imaging was described as before(Stogsdill et al., 2017) and images were acquired at
734 21°C on either an Axioimager M1 (Zeiss) fluorescent microscope with an EC Plan-
735 Neofluar 40× oil NA 1.3 objective (Immersol 518F) and an AxioCAM MRm camera,
736 supported by the AxioVision SE64 software, and a Keyence BZ-X800 microscope with a
737 Nikon S Plan Fluor ELWD ADM 40XC/0.60NA dry/oil objective and a 2/3-inch, 2.83
738 million pixel Peltier-cooled monochrome CCD (colorized with LC filter) camera,
739 supporter by the BZ-X800 analyzer software. Images were acquired by a blinded
740 investigator and analyzed with Sholl analysis in FIJI.

741 **CRISPR genome editing efficiency:**

742 To quantify the percent of frameshift inducing mutations, we cloned all 3 NL2 gRNAs
743 and their respective PAM sequences upstream of and in frame with a GFP coding
744 sequence. In HEK293T (ATCC, RRID:CVCL_4V93) cells we co-transfected the pX601-
745 CMV-SaCas9-U6 gRNA plasmids (containing each NL2 gRNA) with the GFP target
746 plasmid. Three days after transfection, the cells were harvested in 1X MPER (Thermo
747 Scientific), incubated at 4C with end-over-end rotation for 10 minutes and then spun at
748 15,000 x g for 5 minutes. The supernatant was kept for downstream western blot
749 analysis. GFP expression on the resulting western blot was quantified using ImageJ and
750 normalized to GAPDH expression. In this assay, a reduction of GFP expression is
751 interpreted to be genomic cutting by the corresponding gRNA.

752 **In vitro Sholl Analysis:**

753 Sholl Analysis was performed in FIJI (NIH, v1.53c) using the Sholl Analysis plug-in
754 (v4.0.1). The number of intersections is measured with concentric circles at every 1μm
755 starting from a radius of 10μm from the center of the nucleus. Resulting values were
756 then analyzed in R (v4.0.0 and above) using an in-home pipeline which can be found
757 here: https://github.com/Eroglu-Lab/In-Vitro-Sholl. The final graphs are the average of
758 each biological replicate, not of each image. The line graphs were generated using the
759 LOESS method (ggplot2 [Hadley Wickham], stat_smooth function) and the variance
760 (standard error) is represented with the colored lines. The data were analyzed with a
761 linear mixed effects model ANOVA, which accounts for the highly repetitious nature of
762 Sholl analysis data by nesting each Radius measurement within the cell measured
763 (Wilson et al., 2017).

764 **Postnatal astrocyte labeling by electroporation (PALE):**

765 PALE was performed as previously described(Baldwin et al., 2021). Briefly, P0-P1 pups
766 were placed on a glove on ice for < 5 minutes until unresponsive. 1-2μg (in 1-2μl total
767 volume) of plasmid was loaded into a pulled glass pipette containing 1% fast green dye
768 (Sigma F7252). The glass pipette was then inserted into one lateral ventricle of the
769 mouse brain and DNA was injected. Electrodes were then positioned above the visual
770 cortex (positive end) and below the jaw (negative end) and five 50ms pulses of 100V
771 with an interpulse interval of 950ms were applied. Pups recovered on a heating pad and
772 were then returned to the home cage with the dam. Each litter received a random
773 assignment of experimental groups. All animals that recovered after surgery with no

774 visible health issues were kept for the analysis. Animals were transcardially perfused
775 with 4% PFA at P21.

776 **Immunohistochemistry:**

777 Mice were perfused transcardially with 4% PFA and were transferred to 4% PFA
778 overnight before incubation with 30% sucrose in TBS. Coronal sections were collected
779 on a cryostat (Leica) at either 40µm (iBioID, synaptic staining) or 100µm (territory
780 volume and 3D Sholl). Sections were washed 3 times for 10 minutes on a shaker in
781 0.2%(40µm sections) or 0.4%(100µm sections) Triton-X in TBS (TBST). Sections were
782 blocked in 10% Goat serum in TBST for 1 hour on the shaker at room temperature.
783 Primary antibodies: PSD95 (1:300, rabbit, Invitrogen 51-6900, RRID:AB_2533914),
784 Gephyrin (1:500, mouse, Synaptic Systems 147011, RRID:AB_2810215), RFP (1:1000,
785 chicken, Rockland 600-901-379, RRID:AB_10704808, used for synaptic staining),
786 Bassoon (1:500, guinea pig, Synaptic Systems 141318, RRID:AB_2927388), HA
787 (1:200, rat, Roche 11867423001, RRID:AB_390918), RFP [for detecting mCherry CAAX
788 in shRNA PALE experiments] (1:1000, rabbit, Rockland 600-401-379,
789 RRID:AB_2209751), RFP nanobody 568 coupled [for detecting tdTomato in Ai14 mice
790 for NL2 rescue PALE experiments] (1:100, Synaptic Systems,N0404-AF568-L,
791 RRID:AB_2209751), Sox9 (1:1000, Rabbit, Millipore AB5535, RRID:AB_2239761),
792 NeuN (1:1000, Mouse, Millipore MAB377, RRID:AB_2298772) were diluted in fresh
793 blocking buffer and incubated either overnight (40µm) or for 3 nights (100µm). Alexa
794 Fluor or Streptavidin conjugated fluorescent secondaries (Invitrogen: Rabbit 405+
795 RRID:AB_2890548; Mouse IgG1 488 RRID:AB_2535764, Chicken 568
796 RRID:AB_2534098, Guinea Pig 647 RRID:AB_2535867, Rat 488 RRID:AB_2534074,

797 Rabbit 594 RRID:AB_2534095, Streptavidin Alexa Fluor conjugate (Thermo Fisher,
798 S32357)) were diluted in blocking buffer at 1:200 and incubated on tissue for 3 hours at
799 room temperature. DAPI was added in the final wash before mounting. Sections were
800 mounted on glass slides with mounting media (90% Glycerol, 20 mM Tris pH 8.0, 0.5%
801 n-Propyl gallate). Unless specified otherwise, images were acquired at 21°C on a Leica
802 Stellaris 8 Confocal with a 63×/1.40 HC PL APO CS2 (11506350) oil objective (Leica F
803 Immersion liquid [Oil] 11513859) and a Leica K5 sCMOS (14402610) camera,
804 supported by the Leica Application Suite X (LASX, build 4.5.0.25531,
805 RRID:SCR_013673, https://www.leica-microsystems.com/products/microscope-
806 software/p/leica-las-x-ls/) software.

807 **Synapse quantification:**

808 Images for synapse quantification were acquired at 21°C on an Olympus FV3000
809 microscope with an Olympus Plan APO 60× 1.4 NA oil objective (Immoil-f30cc) and a
810 1.64X zoom, supported by the Olympus FV315-SW software. Images were captured in
811 1µm stacks with a 0.34µm step size. We used SynBot(Savage et al., 2024)
812 (https://github.com/Eroglu-Lab/Syn_Bot) in FIJI to quantify the colocalization of Bassoon
813 (visualized by Alexa 594) and Psd95 (excitatory, visualized by Alexa 405+) or Bassoon
814 and Gepyhrin (inhibitory, visualized by Alexa 488) synapses for the entire image using
815 manual thresholding. Using a custom macro in FIJI (https://github.com/Eroglu-
816 Lab/Sakers-et-al-2025), we then cropped the binarized synaptic output images to draw
817 an ROI around the labeled astrocyte and quantify the number of synaptic puncta within
818 and outside the ROI. These synaptic puncta were normalized to the corresponding ROI

819 to obtain a synapse density. The data were analyzed with a linear mixed effects ANOVA
820 in R.

821 **Imaris territory volume and 3D Sholl analysis:**

822 100μm sections were imaged at 21°C on an Olympus FV3000 microscope with an
823 Olympus Plan APO 60× 1.4 NA oil objective (Immoil-f30cc) and a 2× zoom, supported
824 by the Olympus FV315-SW software. Single astrocytes (visualized by Alexa fluor 594
825 secondary antibodies) were captured in a frame in a Z stack at 0.5μm step size to
826 capture the whole astrocyte. Imaris v9.9 (Bitplane) was used to reconstruct images
827 using the filament tracer in 3D. We used two custom extensions to quantify filament
828 complexity (3D Sholl analysis) every 5μm from the cell nucleus [note that this is different
829 from 2D Sholl analysis where a measurement is taken every 1μm from the cell nucleus].
830 A linear mixed model followed by Dunnett's post-hoc test was used to analyze the 3D
831 Sholl data using a custom R script found at: https://github.com/Eroglu-Lab/In-vivo-Sholl-
832 Analysis. The whole astrocyte territory volume was calculated using the Convex Hull
833 function in Imaris on the cell surface. Analysis of territory volume was analyzed in R
834 using a one-way repeated measures ANOVA to account for multiple images taken per
835 animal, followed by Dunnett's post-hoc test.

836 **Adeno-associated virus production:**

837 Purified AAV was produced as described previously(Baldwin et al., 2021). Briefly,
838 HEK293T cells were transfected with pAd-DELTA F6, serotype plasmid AAV PHP.eB,
839 and AAV plasmids (pZac2.1 Turbo ID constructs). Three days after transfection, cells
840 were collected in 15 mM NaCl, 5 mM Tris-HCl, pH 8.5, and lysed with repeat freeze-

841 thaw cycles followed by treatment with Benzonase (Novagen 70664) at 37°C for 30
842 minutes. Lysed cells were pelleted by centrifugation and the supernatant, containing
843 AAV was applied to an Optiprep density gradient (Sigma D1556, 15%, 25%, 40%, and
844 60%) and centrifuged at 67,000 rpm using a Beckman Ti-70 rotor for 1 hour. The AAV-
845 enriched fraction was isolated from between 40% and 60% iodixanol solution and
846 concentrated by repeated washes with sterile PBS in an Amicon Ultra-15 filtration unit
847 (NMWL: 100 kDa, Millipore UFC910008) to a final volume of ~100 µL and aliquoted for
848 storage at −80°C.

849 **In vivo BioID:**

850 Pregnant CD1 dams were ordered from Charles River Laboratories. On P1, pups were
851 anesthetized by hypothermia and subsequently injected intracranially at a depth of 2mm
852 with 1µl equal viral titers of either NL2-Turbo-BirA or Turbo-BirA as previously
853 described. Mice were treated with 0.75mL of 5mM Biotin in sterile PBS via
854 subcutaneous injections once a day from P18 to P20. On P21, mice were sacrificed with
855 200 mg/kg tribromoethanol (avertin) and transcardially perfused with TBS/Heparin for 5
856 minutes to wash out excess biotin. Subsequently, cortices were rapidly dissected in
857 DPBS and flash-frozen in liquid nitrogen.

858 All solutions were made fresh using proteomics-grade chemicals and solvents. Brains
859 were homogenized with approximately 12 strokes in a glass homogenizer and Teflon
860 pestle in 1mL Lysis buffer [50mM Tris/HCl pH7.5, 150mM NaCl, 1mM EDTA with
861 protease inhibitors (Roche)] on ice. An equal volume of 2X RIPA [50mM Tris/HCl pH7.5,
862 150mM NaCl, 1mM EDTA, 0.4% SDS, 2%TritonX100, 2% deoxycholate] was added to
863 the lysates. Lysates were then sonicated (level 9) for 30 seconds (3 x 10s) total,

864 followed by centrifugation at 15,000 RPM for 10 minutes at 4C. The supernatant was
865 transferred to an ultracentrifuge 1.5mL tube (Beckman Coulter) and spun in a TLA-55
866 rotor (Beckman coulter) in an ultracentrifuge at 40,000 RPM for 30 minutes at 4C.
867 Supernatants were transferred to a low-protein binding tube (Eppendorf) and SDS was
868 added to a final concentration of 1%. Samples were then briefly vortexed and heated at
869 45C for 45 mins, cooled on ice, and spun at 15,000RPM for 30 minutes at 4C. 70 µl
870 Neutravidin beads (ThermoFisher 29202) were prepared per condition by washing with
871 1mL of 2X RIPA two times. The samples were transferred to 15mL tubes (1 brain per
872 IP, 3 brains per condition), and washed Neutravidin beads were added to the sample
873 supernatant. 30ul of the supernatant was saved for western blot analysis. The beads
874 and samples were incubated overnight at 4C with rotation. The next day beads were
875 sequentially washed with 1mL of the following solutions for 10 minutes with rotation,
876 followed by two-minute spins: 2% SDS x2, Wash buffer (1% TritonX100, 1%
877 deoxycholate, 25 mM LiCl) x2, 1M NaCl x2, 50mM Ammonium bicarbonate x5. Elution
878 buffer was prepared during the last washes by adding 1.2mg of biotin to 2X sample
879 buffer [4% SDS, 20% glycerol, 0.1% beta-mercaptoethanol, 125mM Tris pH 6.8 to 20mL
880 with keratin-free water]. 70ul of elution buffer was added to the beads and samples
881 were then heated at 60C for 15 minutes to elute bound proteins. The sample was stored
882 at -80C before mass spec analysis, and 5ul of the eluate was saved for western blotting.
883 All washes and elution were done in a tissue culture hood, in sterile conditions to avoid
884 keratin contamination.

885 **Mass spectrometry:**

886 Sample Preparation: The Duke Proteomics Core Facility (DPCF) received 6 samples (3
887 replicates each of two conditions). Samples were reduced with 10 mM dithiothreitol for
888 30 min at 80C and alkylated with 20 mM iodoacetamide for 30 min at room temperature.
889 Next, they were supplemented with a final concentration of 1.2% phosphoric acid and
890 597 µL of S-Trap (Protifi) binding buffer (90% MeOH/100mM TEAB). Proteins were
891 trapped on the S-Trap, digested using 20 ng/µl sequencing grade trypsin (Promega) for
892 1 hr at 47C, and eluted using 50 mM TEAB, followed by 0.2% FA, and lastly using 50%
893 ACN/0.2% FA. All samples were then lyophilized to dryness and resuspended in 12µL
894 1%TFA/2% acetonitrile containing 12.5 fmol/µL yeast alcohol dehydrogenase
895 (ADH_YEAST). A QC Pool was created from 3uL of each sample. All QC Pools were
896 run periodically throughout the acquisition period.

897 Quantitative Analysis, Methods: Quantitative LC/MS/MS was performed on 3 µL of each
898 sample, using a nanoAcquity UPLC system (Waters Corp) coupled to a Thermo
899 Orbitrap Fusion Lumos high-resolution accurate mass tandem mass spectrometer
900 (Thermo) via a nanoelectrospray ionization source. Briefly, the sample was first trapped
901 on a Symmetry C18 20 mm × 180 µm trapping column (5 µl/min at 99.9/0.1 v/v
902 water/acetonitrile), after which the analytical separation was performed using a 1.8 µm
903 Acquity HSS T3 C18 75 µm × 250 mm column (Waters Corp.) with a 90-min linear
904 gradient of 5 to 30% acetonitrile with 0.1% formic acid at a flow rate of 400
905 nanoliters/minute (nL/min) with a column temperature of 55C. Data collection on the
906 Fusion Lumos mass spectrometer was performed in a data-dependent acquisition
907 (DDA) mode of acquisition with a r=120,000 (@ m/z 200) full MS scan from m/z 375 –
908 1500 with a target AGC value of 2e5 ions. MS/MS scans were acquired at a Rapid scan

909 rate (Ion Trap) with an AGC target of 5e3 ions and a max injection time of 100 ms. The
910 total cycle time for MS and MS/MS scans was 2 sec. A 20s dynamic exclusion was
911 employed to increase the depth of coverage. The total analysis cycle time for each
912 sample injection was approximately 2 hours. Following 9 total UPLC-MS/MS analyses
913 (excluding conditioning runs, but including 3 replicate QC Pool), data was imported into
914 Proteome Discoverer 2.3 (Thermo Scientific Inc.), and analyses were aligned based on
915 the accurate mass and retention time of detected ions ("features") using Minora Feature
916 Detector algorithm in Proteome Discoverer. Relative peptide abundance was calculated
917 based on the area-under-the-curve (AUC) of the selected ion chromatograms of the
918 aligned features across all runs. The MS/MS data was searched against the SwissProt
919 M. musculus database (downloaded in Apr2017) and an equal number of reversed-
920 sequence "decoys" for false discovery rate determination. Mascot Distiller and Mascot
921 Server (v 2.5, Matrix Sciences) were utilized to produce fragment ion spectra and to
922 perform the database searches. Database search parameters included fixed
923 modifications on Cys (carbamidomethyl) and variable modifications on Meth (oxidation)
924 and Asn and Gln (deamidation). Peptide Validator and Protein FDR Validator nodes in
925 Proteome Discoverer were used to annotate the data at a maximum 1% protein false
926 discovery rate.

927 *Statistical analysis of iBioID data:*

928 In vivo BioID has an inherently high background in mass spectrometry due to the time
929 necessary for biotin to accumulate in the system, and the diffuse nature of AMP-biotin.
930 We controlled for this background using a soluble (non-bait) TurboID enzyme in both
931 astrocytes and neurons, as this would accurately replicate the high background in bait

932 conditions. Further, to account for differences in expression due to the size differenced
933 of soluble TurboID and NL-tagged TurboID, we employed a robust-mean normalization
934 which excludes the top and bottom 10% of signal intensities and mitigates the
935 influences of outliers. The BioID datasets were generated from distinct viral constructs
936 and cellular contexts, thus necessitating an enrichment-over-control design. To do so,
937 we calculated the fold changes and used a two-tailed heteroscedastic t-test on log2-
938 transformed data comparing the NL2 and Turbo BioID groups, and performed FDR
939 correction to obtain high-confidence putative interactors.

940 **Western blotting:**

941 iBioID: 5ul of IP eluate and 30ul of sonicated lysate were run on a 4-15% Mini-Protean
942 precast gel (BioRad). After transfer, membranes were blocked in Odyssey blocking
943 buffer (LI-COR) diluted in PBS (1:1) followed by incubation in the same buffer with
944 Alexa 680 conjugated streptavidin (Invitrogen). Membranes were imaged on a LI-COR
945 Odyssey CLx. Densitometry analysis was performed in ImageJ (NIH v1.54f)

946 All other blots: Equal protein (measured by Bicinchoninic Acid Protein Assay (BCA,
947 Pierce)) was loaded on a 4-15% Mini-Protean precast gel (BioRad). In the case of
948 immunoprecipitations, input samples were loaded as an equal percentage of total
949 sample homogenate, and the entirety of the IP eluate was run per lane. Gels were
950 transferred using a Power Blotter System (Invitrogen) and then blocked in a Blocking
951 Buffer for Fluorescent Western Blotting (Rockland, MB-070) diluting in PBS (1:1). The
952 following primary antibodies were used for blotting: Rabbit anti-Nedd4l (Cell Signaling
953 Technology, 4013S, 1:1000, RRID:AB_1904063), Rabbit anti-V5 (Cell Signaling
954 Technology, 13202S, 1:500, RRID:AB_2687461), Chicken anti-HA (Aves Labs, ET-

955 HA100, 1:2000, RRID:AB_2313511), Rabbit anti-GFP (Novus Biologicals, NB600-308,
956 1:1000, RRID:AB_10003058), Mouse anti-Gapdh (Abcam, ab8245, 1:2500,
957 RRID:AB_2107448), Mouse anti-Actin (Sigma-Aldrich, A5441, 1:2000,
958 RRID:AB_476744) diluted in blocking buffer. LI-COR 680 or 800 fluorescent secondary
959 antibodies (Chicken 800 RRID:AB_10974977; Rabbit 800 RRID:AB_621848; Mouse
960 800 RRID:AB_621842, Rabbit 680 RRID:AB_621845, Chicken 680 RRID:AB_1850018)
961 were diluted 1:2500 in blocking buffer and blots were imaged on a LI-COR Odyssey
962 CLx.

963 **Lentivirus production and transduction:**

964 8-10 million 293T cells were plated in a T-75 culture flask and transfected using
965 Xtremegene HP Transfection Reagent (Roche, 06366236001) with the following
966 plasmids: pLKO.1 puromycin-resistant shRNA plasmids (described above), VSVG (an
967 envelope plasmid), and dR8.91 packaging plasmid. One day post-transfection, the
968 media was replaced with astrocyte growth media, and lentivirus was collected on days 2
969 and 3 and filtered through a 40μm syringe filter. Media was tested for lentiviral particles
970 using Lenti-X Go Stix (Takara, 631280). Astrocytes were treated with 500μl of lentiviral
971 media supernatant, and 1μg/mL polybrene on DIV8. On DIV10, astrocytes were treated
972 with 1μg/mL puromycin every other day until a non-transduced well was completely
973 dead. Cells were lysed for qPCR as described below. Cells collected for western blot
974 were collected in T-PER (Thermo Scientific, 78510) and protein was measured using a
975 BCA protein assay (Thermo Scientific, 23227).

976 **Gene ontology analysis:**

977 Gene ontology analysis was performed in R using the package clusterProfiler v4.6.2(Wu
978 et al., 2021). Proteins from iBioID lists that were at least 1.5 fold enriched at a p-value of
979 <0.05, compared to respective controls described in legends, were subjected to
980 Biological Processes enrichment. Resulting output was reduced using the simplify
981 function in clusterProfiler. The top 5-10 categories (sorted by adjusted p-value) were
982 plotted in R. The entire enrichment can be found in Supplemental Dataset 2.

983 **Immunoprecipitation:**

984 4 million 293T cells (ATCC, RRID:CVCL_4V93) (passage #8-15) were plated in 10cm
985 dishes and then transfected the next day with 2.5µg of each plasmid using the
986 Xtremegene HP Transfection Reagent (Roche, 06366236001) according to the
987 manufacturer's protocol. 48 hours post transfection cells were washed with 1X TBS
988 supplemented with calcium and magnesium and pelleted. Cell pellets were
989 resuspended in 400µl of lysis buffer (25mM Tris pH 7.4, 1mM Calcium Chloride, 1mM
990 Magnesium Chloride, 150mM Sodium Chloride, 0.5% NP-40, 1X EDTA-free protease
991 inhibitor cocktail (Roche)) and centrifuged at 20,000xg for 10 minutes. 5% of the
992 supernatant was saved for input samples, and the remaining lysate was diluted with
993 lysis buffer without NP-40 for IP. Lysate was added to 30µl of magnetic anti-HA beads
994 (Pierce, 88836) overnight at 4C with rotation. Beads were collected on a magnetic rack
995 and washed 3 times with wash buffer (25mM Tris pH 7.4, 1mM Calcium Chloride, 1mM
996 Magnesium Chloride, 150mM Sodium Chloride, 0.1% NP-40, 1X EDTA-free protease
997 inhibitor cocktail (Roche)). Beads were eluted with 2X Laemmli buffer (Bio-Rad,
998 1610737) at 42C for 15 minutes and then denatured with 5% β-mercaptoethanol at 45C
999 for 45 minutes before loading on SDS-PAGE. Bands were quantified via densitometry

1000 (ImageJ). Co-IP bands were normalized to the IP band of bait protein (Figure 6, HA-
1001 NLs). Paired Student's t-tests were used to compare differences across condition, using
1002 biological replicates as pairs.

1003 **Ubiquitination assay:**

1004 293T cells were transfected as indicated in the immunoprecipitation subsection. 48
1005 hours post-transfection, cells were treated with 25μM MG-132 (Sigma-Aldrich, 474790)
1006 for 2-4 hours to block the proteasome. Cells were washed 3 times in ice-cold 1X TBS
1007 supplemented with magnesium, calcium, and N-ethylmaleimide (NEM) (Sigma-Aldrich,
1008 E3876) to block deubiquitinases and then pelleted. Cells were resuspended in 1X RIPA
1009 buffer with SDS (50 mM Tris-HCl pH 7.4, 150 mM NaCl, 1% NP-40, 0.5% Sodium
1010 Deoxycholate, 1% Sodium dodecyl sulfate, supplemented with 1X protease inhibitor and
1011 20mM NEM) and then boiled for 5 minutes to disrupt protein-protein interactions. The
1012 lysates were diluted 10X with 1X RIPA without SDS and incubated on a rotator at 4C for
1013 1 hour. The lysates were then pelleted at 15,000xg for 15 minutes and the supernatant
1014 was added to magnetic anti-HA beads, and 5% of the supernatant was collected for
1015 input fraction. Elution was performed identically to the immunoprecipitation subsection
1016 above. For ubiquitination assay in primary rat astrocytes, 5 million DIV7 astrocytes
1017 (prepared as described above) were nucleofected with the Basic Glial Cells
1018 Nucleofection Kit (Lonza) and 5ug of each plasmid. 24 hours after nucleofection, the
1019 media was changed to remove dead cells and nucleofection solution. Ubiquitination IP
1020 was performed 3 days after nucleofection in the same manner as 293T cells.

1021 **Degradation assay:**

1022 350,000 HEK 293T cells were plated into wells of a 6-well plate and then transfected
1023 one day later with 1µg of each plasmid via Xtremegene HP Transfection Reagent
1024 reagent (Roche #06366236001). 48 hours later cells were treated with cycloheximide
1025 (100µg/mL). At each time point, the collected cells were washed with 1X TBS with
1026 magnesium and calcium, pelleted, and then resuspended in 1X RIPA (Sigma-Aldrich)
1027 supplemented with protease inhibitors. Lysates were incubated at 4C with rotation for
1028 40 minutes, centrifuged at 20,000xg at 4C and supernatants were saved for protein
1029 quantitation via BCA. 5µg of total protein was loaded on a 4-15% SDS-PAGE. Three
1030 independent cultures were used for statistical analysis.

1031 **Statistics:**

1032 Experiments were randomized where applicable and analyses were run by an
1033 experimenter blind to the condition. All in vitro experiments were performed at least 3
1034 times (3 different cultures), with 20+ cells imaged per replicate. Note that some
1035 conditions were plotted across several figures (i.e. shNL2 in Figure S1, Figure 1; shNL2
1036 + HA-NL2 Figure 1D and F and S1, and shNL2 in Figure 5), as experiments were done
1037 in parallel. All analyses were done in R (v4.0.0 and above). An R script with
1038 reproducible data can be found at the following links for both in vitro analysis
1039 (https://github.com/Eroglu-Lab/In-Vitro-Sholl) and in vivo analysis
1040 (https://github.com/Eroglu-Lab/In-vivo-Sholl-Analysis). Sholl analysis statistical analysis
1041 was performed using a linear mixed effects ANOVA which accurately accounts for the
1042 multilevel and repetitive nature of the data(Wilson et al., 2017). Statistical analyses were
1043 performed using N of independent culture or animal rather than image to avoid

1044 pseudoreplication artifacts. Specific details on sample size, and test applied can be

1045 found in the figure legends and Methods subsections and in Table S1.

1046

Data availability statement

The mass spectrometry proteomics data have been deposited to the ProteomeXchange Consortium via the PRIDE(Perez-Riverol et al., 2022) partner repository with the dataset identifier PXD049185. All data in this manuscript can be found in the attached Source Data file, and all original images can be accessed via Duke Digital Repository: https://doi.org/10.7924/r4r500.

Conflict of Interest Statement

The authors declare no competing financial interests.

Author contributions

Conceptualization: Kristina Sakers and Cagla Eroglu; Investigation: Kristina Sakers, Juan J. Ramirez, Nimrod Elazar, Leykashree Nagendren; Methodology: Kristina Sakers, Cagla Eroglu; Data curation: Kristina Sakers; Formal analysis: Kristina Sakers, Erik Soderblom; Writing: Kristina Sakers, Cagla Eroglu. Project administration: Kristina Sakers; Supervision: Cagla Eroglu; Funding acquisition: Cagla Eroglu, Kristina Sakers, Nimrod Elazar and Juan J. Ramirez.

1062 ## REFERENCES

1063 Ackerman, S.D., N.A. Perez-Catalan, M.R. Freeman, and C.Q. Doe. 2021. Astrocytes close a motor circuit
1064 critical period. *Nature*. 592:414–420. doi:10.1038/s41586-021-03441-2.

1065 Altas, B., H.-J. Rhee, A. Ju, H.C. Solís, S. Karaca, J. Winchenbach, O. Kaplan-Arabaci, M. Schwark, M.C.
1066 Ambrozkiewicz, C. Lee, L. Spieth, G.L. Wieser, V.K. Chaugule, I. Majoul, M.A. Hassan, R. Goel,
1067 S.M. Wojcik, N. Koganezawa, K. Hanamura, D. Rotin, A. Pichler, M. Mitkovski, L. de Hoz, A.
1068 Poulopoulos, H. Urlaub, O. Jahn, G. Saher, N. Brose, J. Rhee, and H. Kawabe. 2024. Nedd4-2-
1069 dependent regulation of astrocytic Kir4.1 and Connexin43 controls neuronal network activity. *J.*
1070 *Cell Biol.* 223:e201902050. doi:10.1083/jcb.201902050.

1071 Babaev, O., P. Botta, E. Meyer, C. Müller, H. Ehrenreich, N. Brose, A. Lüthi, and D. Krueger-Burg. 2016.
1072 Neuroligin 2 deletion alters inhibitory synapse function and anxiety-associated neuronal
1073 activation in the amygdala. *Neuropharmacology*. 100:56–65.
1074 doi:10.1016/j.neuropharm.2015.06.016.

1075 Baldwin, K.T., K.K. Murai, and B.S. Khakh. 2023. Astrocyte morphology. *Trends Cell Biol.* S0962-
1076 8924(23)00204–0. doi:10.1016/j.tcb.2023.09.006.

1077 Baldwin, K.T., C.X. Tan, S.T. Strader, C. Jiang, J.T. Savage, X. Elorza-Vidal, X. Contreras, T. Rülicke, S.
1078 Hippenmeyer, R. Estévez, R.-R. Ji, and C. Eroglu. 2021. HepaCAM controls astrocyte self-
1079 organization and coupling. *Neuron*. 109:2427-2442.e10. doi:10.1016/j.neuron.2021.05.025.

1080 Barrow, S.L., J.R. Constable, E. Clark, F. El-Sabeawy, A.K. McAllister, and P. Washbourne. 2009.
1081 Neuroligin1: a cell adhesion molecule that recruits PSD-95 and NMDA receptors by distinct
1082 mechanisms during synaptogenesis. *Neural Develop.* 4:17. doi:10.1186/1749-8104-4-17.

1083 Binda, C.S., Y. Nakamura, J.M. Henley, and K.A. Wilkinson. 2019. Sorting nexin 27 rescues neuroligin 2
1084 from lysosomal degradation to control inhibitory synapse number. *Biochem. J.* 476:293–306.
1085 doi:10.1042/BCJ20180504.

1086 Boisvert, M.M., G.A. Erikson, M.N. Shokhirev, and N.J. Allen. 2018. The Aging Astrocyte Transcriptome
1087 from Multiple Regions of the Mouse Brain. *Cell Rep.* 22:269–285.
1088 doi:10.1016/j.celrep.2017.12.039.

1089 Booth, H.D.E., W.D. Hirst, and R. Wade-Martins. 2017. The Role of Astrocyte Dysfunction in Parkinson's
1090 Disease Pathogenesis. *Trends Neurosci.* 40:358–370. doi:10.1016/j.tins.2017.04.001.

1091 Branon, T.C., J.A. Bosch, A.D. Sanchez, N.D. Udeshi, T. Svinkina, S.A. Carr, J.L. Feldman, N. Perrimon, and
1092 A.Y. Ting. 2018. Efficient proximity labeling in living cells and organisms with TurboID. *Nat.*
1093 *Biotechnol.* 36:880–887. doi:10.1038/nbt.4201.

1094 Bruce, M.C., V. Kanelis, F. Fouladkou, A. Debonneville, O. Staub, and D. Rotin. 2008. Regulation of
1095 Nedd4-2 self-ubiquitination and stability by a PY motif located within its HECT-domain. *Biochem.*
1096 *J.* 415:155–163. doi:10.1042/BJ20071708.

1097 Bushong, E.A., M.E. Martone, and M.H. Ellisman. 2004. Maturation of astrocyte morphology and the
1098 establishment of astrocyte domains during postnatal hippocampal development. *Int. J. Dev.*
1099 *Neurosci.* 22:73–86. doi:10.1016/j.ijdevneu.2003.12.008.

1100 Bushong, E.A., M.E. Martone, Y.Z. Jones, and M.H. Ellisman. 2002. Protoplasmic astrocytes in CA1
1101 stratum radiatum occupy separate anatomical domains. *J. Neurosci. Off. J. Soc. Neurosci.*
1102 22:183–192. doi:10.1523/JNEUROSCI.22-01-00183.2002.

1103 Chanda, S., W.D. Hale, B. Zhang, M. Wernig, and T.C. Südhof. 2017. Unique versus Redundant Functions
1104 of Neuroligin Genes in Shaping Excitatory and Inhibitory Synapse Properties. *J. Neurosci. Off. J.*
1105 *Soc. Neurosci.* 37:6816–6836. doi:10.1523/JNEUROSCI.0125-17.2017.

1106 Chen, H.I., A. Einbond, S.J. Kwak, H. Linn, E. Koepf, S. Peterson, J.W. Kelly, and M. Sudol. 1997.
1107 Characterization of the WW domain of human yes-associated protein and its polyproline-
1108 containing ligands. *J. Biol. Chem.* 272:17070–17077. doi:10.1074/jbc.272.27.17070.

1109 Chih, B., H. Engelman, and P. Scheiffele. 2005. Control of excitatory and inhibitory synapse formation by
1110 neuroligins. *Science*. 307:1324–1328. doi:10.1126/science.1107470.

1111 Chih, B., L. Gollan, and P. Scheiffele. 2006. Alternative splicing controls selective trans-synaptic
1112 interactions of the neuroligin-neurexin complex. *Neuron*. 51:171–178.
1113 doi:10.1016/j.neuron.2006.06.005.

1114 Clarke, L.E., S.A. Liddelow, C. Chakraborty, A.E. Münch, M. Heiman, and B.A. Barres. 2018. Normal aging
1115 induces A1-like astrocyte reactivity. *Proc. Natl. Acad. Sci.* 115:E1896–E1905.
1116 doi:10.1073/pnas.1800165115.

1117 Concordet, J.-P., and M. Haeussler. 2018. CRISPOR: intuitive guide selection for CRISPR/Cas9 genome
1118 editing experiments and screens. *Nucleic Acids Res.* 46:W242–W245. doi:10.1093/nar/gky354.

1119 Endo, F., A. Kasai, J.S. Soto, X. Yu, Z. Qu, H. Hashimoto, V. Gradinaru, R. Kawaguchi, and B.S. Khakh. 2022.
1120 Molecular basis of astrocyte diversity and morphology across the CNS in health and disease.
1121 *Science*. 378:eadc9020. doi:10.1126/science.adc9020.

1122 Farhy-Tselnicker, I., M.M. Boisvert, H. Liu, C. Dowling, G.A. Erikson, E. Blanco-Suarez, C. Farhy, M.N.
1123 Shokhirev, J.R. Ecker, and N.J. Allen. 2021. Activity-dependent modulation of synapse-regulating
1124 genes in astrocytes. *eLife*. 10:e70514. doi:10.7554/eLife.70514.

1125 Farizatto, K.L.G., and K.T. Baldwin. 2023. Astrocyte-synapse interactions during brain development. *Curr.*
1126 *Opin. Neurobiol.* 80:102704. doi:10.1016/j.conb.2023.102704.

1127 Giannone, G., M. Mondin, D. Grillo-Bosch, B. Tessier, E. Saint-Michel, K. Czöndör, M. Sainlos, D. Choquet,
1128 and O. Thoumine. 2013. Neurexin-1β Binding to Neuroligin-1 Triggers the Preferential
1129 Recruitment of PSD-95 versus Gephyrin through Tyrosine Phosphorylation of Neuroligin-1. *Cell*
1130 *Rep.* 3:1996–2007. doi:10.1016/j.celrep.2013.05.013.

1131 Goel, K., and J.E. Ploski. 2022. RISC-y Business: Limitations of Short Hairpin RNA-Mediated Gene
1132 Silencing in the Brain and a Discussion of CRISPR/Cas-Based Alternatives. *Front. Mol. Neurosci.*
1133 15. doi:10.3389/fnmol.2022.914430.

1134 Golf, S.R., J.H. Trotter, J. Wang, G. Nakahara, X. Han, M. Wernig, and T.C. Südhof. 2025. Deletion of
1135 Neuroligins from Astrocytes Does Not Detectably Alter Synapse Numbers or Astrocyte
1136 Cytoarchitecture by Maturity. *eLife*. 12. doi:10.7554/eLife.87589.3.

1137 Gupta, S., J.A. Stamatoyannopoulos, T.L. Bailey, and W.S. Noble. 2007. Quantifying similarity between
1138 motifs. *Genome Biol.* 8:R24. doi:10.1186/gb-2007-8-2-r24.

1139 Gutmann, D.H., A. Loehr, Y. Zhang, J. Kim, M. Henkemeyer, and A. Cashen. 1999. Haploinsufficiency for
1140 the neurofibromatosis 1 (NF1) tumor suppressor results in increased astrocyte proliferation.
1141 *Oncogene*. 18:4450–4459. doi:10.1038/sj.onc.1202829.

1142 Halff, E.F., B.R. Szulc, F. Lesept, and J.T. Kittler. 2019. SNX27-Mediated Recycling of Neuroligin-2
1143 Regulates Inhibitory Signaling. *Cell Rep.* 29:2599-2607.e6. doi:10.1016/j.celrep.2019.10.096.

1144 Hatstat, A.K., M.D. Pupi, and D.G. McCafferty. 2021. Predicting PY motif-mediated protein-protein
1145 interactions in the Nedd4 family of ubiquitin ligases. *PLOS ONE*. 16:e0258315.
1146 doi:10.1371/journal.pone.0258315.

1147 Holt, L.M., R.D. Hernandez, N.L. Pacheco, B. Torres Ceja, M. Hossain, and M.L. Olsen. 2019. Astrocyte
1148 morphogenesis is dependent on BDNF signaling via astrocytic TrkB.T1. *eLife*. 8:e44667.
1149 doi:10.7554/eLife.44667.

1150 Hunker, A.C., and L.S. Zweifel. 2020. Protocol to Design, Clone, and Validate sgRNAs for *In Vivo* Reverse
1151 Genetic Studies. *STAR Protoc.* 1:100070. doi:10.1016/j.xpro.2020.100070.

1152 Ilsley, J.L., M. Sudol, and S.J. Winder. 2002. The WW domain: linking cell signalling to the membrane
1153 cytoskeleton. *Cell. Signal.* 14:183–189.

1154 Irie, M., Y. Hata, M. Takeuchi, K. Ichtchenko, A. Toyoda, K. Hirao, Y. Takai, T.W. Rosahl, and T.C. Südhof.
1155 1997. Binding of Neuroligins to PSD-95. *Science*. 277:1511–1515.
1156 doi:10.1126/science.277.5331.1511.

1157 Jamain, S., H. Quach, C. Betancur, M. Råstam, C. Colineaux, I.C. Gillberg, H. Söderström, B. Giros, M.
1158 Leboyer, C. Gillberg, and T. Bourgeron. 2003. Mutations of the X-linked genes encoding
1159 neuroligins NLGN3 and NLGN4 are associated with autism. *Nat. Genet.* 34:27–29.
1160 doi:10.1038/ng1136.

1161 Kang, Y., Y. Ge, R.M. Cassidy, V. Lam, L. Luo, K.-M. Moon, R. Lewis, R.S. Molday, R.O.L. Wong, L.J. Foster,
1162 and A.M. Craig. 2014. A Combined Transgenic Proteomic Analysis and Regulated Trafficking of
1163 Neuroligin-2. *J. Biol. Chem.* 289:29350–29364. doi:10.1074/jbc.M114.549279.

1164 Kasanov, J., G. Pirozzi, A.J. Uveges, and B.K. Kay. 2001. Characterizing Class I WW domains defines key
1165 specificity determinants and generates mutant domains with novel specificities. *Chem. Biol.*
1166 8:231–241.

1167 Kato, Y., M. Ito, K. Kawai, K. Nagata, and M. Tanokura. 2002. Determinants of Ligand Specificity in
1168 Groups I and IV WW Domains as Studied by Surface Plasmon Resonance and Model Building *. *J.*
1169 *Biol. Chem.* 277:10173–10177. doi:10.1074/jbc.M110490200.

1170 Kato, Y., K. Nagata, M. Takahashi, L. Lian, J.J. Herrero, M. Sudol, and M. Tanokura. 2004. Common
1171 mechanism of ligand recognition by group II/III WW domains: redefining their functional
1172 classification. *J. Biol. Chem.* 279:31833–31841. doi:10.1074/jbc.M404719200.

1173 Kirkeby, S., D. Moe, T.C. Bøg-Hansen, and C.J.F. van Noorden. 1993. Biotin carboxylases in mitochondria
1174 and the cytosol from skeletal and cardiac muscle as detected by avidin binding. *Histochemistry*.
1175 100:415–421. doi:10.1007/BF00267821.

1176 Lavialle, M., G. Aumann, E. Anlauf, F. Pröls, M. Arpin, and A. Derouiche. 2011. Structural plasticity of
1177 perisynaptic astrocyte processes involves ezrin and metabotropic glutamate receptors. *Proc.*
1178 *Natl. Acad. Sci. U. S. A.* 108:12915–12919. doi:10.1073/pnas.1100957108.

1179 Lee, D.-E., J.E. Yoo, J. Kim, S. Kim, S. Kim, H. Lee, and H. Cheong. 2020. NEDD4L downregulates
1180 autophagy and cell growth by modulating ULK1 and a glutamine transporter. *Cell Death Dis.*
1181 11:1–17. doi:10.1038/s41419-020-2242-5.

1182 Lee, K.Y., K.A. Jewett, H.J. Chung, and N.-P. Tsai. 2018. Loss of fragile X protein FMRP impairs
1183 homeostatic synaptic downscaling through tumor suppressor p53 and ubiquitin E3 ligase Nedd4-
1184 2. *Hum. Mol. Genet.* 27:2805–2816. doi:10.1093/hmg/ddy189.

1185 Lee, Y., A. Messing, M. Su, and M. Brenner. 2008. GFAP promoter elements required for region-specific
1186 and astrocyte-specific expression. *Glia*. 56:481–493. doi:10.1002/glia.20622.

1187 Letellier, M., Z. Szíber, I. Chamma, C. Saphy, I. Papasideri, B. Tessier, M. Sainlos, K. Czöndör, and O.
1188 Thoumine. 2018. A unique intracellular tyrosine in neuroligin-1 regulates AMPA receptor
1189 recruitment during synapse differentiation and potentiation. *Nat. Commun.* 9:3979.
1190 doi:10.1038/s41467-018-06220-2.

1191 Li, J., T.G. Miramontes, T. Czopka, and K.R. Monk. 2024. Synaptic input and Ca2+ activity in zebrafish
1192 oligodendrocyte precursor cells contribute to myelin sheath formation. *Nat. Neurosci.*
1193 doi:10.1038/s41593-023-01553-8.

1194 Liu, X., H. Zhang, B. Zhang, J. Tu, X. Li, and Y. Zhao. 2021. Nedd4-2 haploinsufficiency in mice causes
1195 increased seizure susceptibility and impaired Kir4.1 ubiquitination. *Biochim. Biophys. Acta Mol.*
1196 *Basis Dis.* 1867:166128. doi:10.1016/j.bbadis.2021.166128.

1197 Loh, K.H., P.S. Stawski, A.S. Draycott, N.D. Udeshi, E.K. Lehrman, D.K. Wilton, T. Svinkina, T.J. Deerinck,
1198 M.H. Ellisman, B. Stevens, S.A. Carr, and A.Y. Ting. 2016. Proteomic Analysis of Unbounded
1199 Cellular Compartments: Synaptic Clefts. *Cell*. 166:1295-1307.e21.
1200 doi:10.1016/j.cell.2016.07.041.

1201 Minegishi, S., T. Ishigami, T. Kino, L. Chen, R. Nakashima-Sasaki, N. Araki, K. Yatsu, M. Fujita, and S.
1202 Umemura. 2016. An isoform of Nedd4-2 is critically involved in the renal adaptation to high salt
1203 intake in mice. *Sci. Rep.* 6:27137. doi:10.1038/srep27137.

1204 Molotkov, D., S. Zobova, J.M. Arcas, and L. Khiroug. 2013. Calcium-induced outgrowth of astrocytic
1205 peripheral processes requires actin binding by Profilin-1. *Cell Calcium*. 53:338–348.
1206 doi:10.1016/j.ceca.2013.03.001.

1207 Mukhopadhyay, D., and H. Riezman. 2007. Proteasome-independent functions of ubiquitin in
1208 endocytosis and signaling. *Science*. 315:201–205. doi:10.1126/science.1127085.

1209 Na, C.H., D.R. Jones, Y. Yang, X. Wang, Y. Xu, and J. Peng. 2012. Synaptic Protein Ubiquitination in Rat
1210 Brain Revealed by Antibody-based Ubiquitome Analysis. *J. Proteome Res.* 11:4722–4732.
1211 doi:10.1021/pr300536k.

1212 Nagaki, K., H. Yamamura, S. Shimada, T. Saito, S. Hisanaga, M. Taoka, T. Isobe, and T. Ichimura. 2006. 14-
1213 3-3 Mediates phosphorylation-dependent inhibition of the interaction between the ubiquitin E3
1214 ligase Nedd4-2 and epithelial Na+ channels. *Biochemistry*. 45:6733–6740.
1215 doi:10.1021/bi052640q.

1216 Nguyen, Q.-A., M.E. Horn, and R.A. Nicoll. 2016. Distinct roles for extracellular and intracellular domains
1217 in neuroligin function at inhibitory synapses. *eLife*. 5. doi:10.7554/eLife.19236.

1218 Oberheim, N.A., X. Wang, S. Goldman, and M. Nedergaard. 2006. Astrocytic complexity distinguishes the
1219 human brain. *Trends Neurosci.* 29:547–553. doi:10.1016/j.tins.2006.08.004.

1220 Parente, D.J., C. Garriga, B. Baskin, G. Douglas, M.T. Cho, G.C. Araujo, and M. Shinawi. 2017. Neuroligin 2
1221 nonsense variant associated with anxiety, autism, intellectual disability, hyperphagia, and
1222 obesity. *Am. J. Med. Genet. A.* 173:213–216. doi:10.1002/ajmg.a.37977.

1223 Perez-Riverol, Y., J. Bai, C. Bandla, D. García-Seisdedos, S. Hewapathirana, S. Kamatchinathan, D.J.
1224 Kundu, A. Prakash, A. Frericks-Zipper, M. Eisenacher, M. Walzer, S. Wang, A. Brazma, and J.A.
1225 Vizcaíno. 2022. The PRIDE database resources in 2022: a hub for mass spectrometry-based
1226 proteomics evidences. *Nucleic Acids Res.* 50:D543–D552. doi:10.1093/nar/gkab1038.

1227 Pirozzi, G., S.J. McConnell, A.J. Uveges, J.M. Carter, A.B. Sparks, B.K. Kay, and D.M. Fowlkes. 1997.
1228 Identification of novel human WW domain-containing proteins by cloning of ligand targets. *J.*
1229 *Biol. Chem.* 272:14611–14616. doi:10.1074/jbc.272.23.14611.

1230 Poulopoulos, A., G. Aramuni, G. Meyer, T. Soykan, M. Hoon, T. Papadopoulos, M. Zhang, I. Paarmann, C.
1231 Fuchs, K. Harvey, P. Jedlicka, S.W. Schwarzacher, H. Betz, R.J. Harvey, N. Brose, W. Zhang, and F.
1232 Varoqueaux. 2009. Neuroligin 2 Drives Postsynaptic Assembly at Perisomatic Inhibitory Synapses
1233 through Gephyrin and Collybistin. *Neuron*. 63:628–642. doi:10.1016/j.neuron.2009.08.023.

1234 Poulopoulos, A., T. Soykan, L.P. Tuffy, M. Hammer, F. Varoqueaux, and N. Brose. 2012.
1235 Homodimerization and isoform-specific heterodimerization of neuroligins. *Biochem. J.* 446:321–
1236 330. doi:10.1042/BJ20120808.

1237 Preman, P., M. Alfonso-Triguero, E. Alberdi, A. Verkhratsky, and A.M. Arranz. 2021. Astrocytes in
1238 Alzheimer's Disease: Pathological Significance and Molecular Pathways. *Cells*. 10:540.
1239 doi:10.3390/cells10030540.

1240 Rodrigues, D.C., M. Mufteev, R.J. Weatheritt, U. Djuric, K.C.H. Ha, P.J. Ross, W. Wei, A. Piekna, M.A.
1241 Sartori, L. Byres, R.S.F. Mok, K. Zaslavsky, P. Pasceri, P. Diamandis, Q. Morris, B.J. Blencowe, and
1242 J. Ellis. 2020. Shifts in Ribosome Engagement Impact Key Gene Sets in Neurodevelopment and
1243 Ubiquitination in Rett Syndrome. *Cell Rep.* 30:4179-4196.e11. doi:10.1016/j.celrep.2020.02.107.

1244 Rothstein, J.D., M. Van Kammen, A.I. Levey, L.J. Martin, and R.W. Kuncl. 1995. Selective loss of glial
1245 glutamate transporter GLT-1 in amyotrophic lateral sclerosis. *Ann. Neurol.* 38:73–84.
1246 doi:10.1002/ana.410380114.

1247 Roux, K.J., D.I. Kim, M. Raida, and B. Burke. 2012. A promiscuous biotin ligase fusion protein identifies
1248 proximal and interacting proteins in mammalian cells. *J. Cell Biol.* 196:801–810.
1249 doi:10.1083/jcb.201112098.

1250 Savage, J.T., J.J. Ramirez, W.C. Risher, Y. Wang, D. Irala, and C. Eroglu. 2024. SynBot is an open-source
1251 image analysis software for automated quantification of synapses. *Cell Rep. Methods*. 4:100861.
1252 doi:10.1016/j.crmeth.2024.100861.

1253 Scheiffele, P., J. Fan, J. Choih, R. Fetter, and T. Serafini. 2000. Neuroligin expressed in nonneuronal cells
1254 triggers presynaptic development in contacting axons. *Cell*. 101:657–669.

1255 Schnell, E., A.L. Bensen, E.K. Washburn, and G.L. Westbrook. 2012. Neuroligin-1 overexpression in
1256 newborn granule cells in vivo. *PloS One*. 7:e48045. doi:10.1371/journal.pone.0048045.

1257 Schnell, E., T.H. Long, A.L. Bensen, E.K. Washburn, and G.L. Westbrook. 2014. Neuroligin-1 knockdown
1258 reduces survival of adult-generated newborn hippocampal neurons. *Front. Neurosci.* 8.

1259 Shipman, S.L., and R.A. Nicoll. 2012. Dimerization of postsynaptic neuroligin drives synaptic assembly via
1260 transsynaptic clustering of neurexin. *Proc. Natl. Acad. Sci.* 109:19432–19437.
1261 doi:10.1073/pnas.1217633109.

1262 Shipman, S.L., E. Schnell, T. Hirai, B.-S. Chen, K.W. Roche, and R.A. Nicoll. 2011. Functional dependence
1263 of neuroligin on a new non-PDZ intracellular domain. *Nat. Neurosci.* 14:718–726.
1264 doi:10.1038/nn.2825.

1265 Singh, S.K., J.A. Stogsdill, N.S. Pulimood, H. Dingsdale, Y.H. Kim, L.-J. Pilaz, I.H. Kim, A.C. Manhaes, W.S.
1266 Rodrigues Jr., A. Pamukcu, E. Enustun, Z. Ertuz, P. Scheiffele, S.H. Soderling, D.L. Silver, R.-R. Ji,
1267 A.E. Medina, and C. Eroglu. 2016. Astrocytes Assemble Thalamocortical Synapses by Bridging
1268 NRX1α and NL1 via Hevin. *Cell*. 164:183–196. doi:10.1016/j.cell.2015.11.034.

1269 Soto, J.S., Y. Jami-Alahmadi, J. Chacon, S.L. Moye, B. Diaz-Castro, J.A. Wohlschlegel, and B.S. Khakh.
1270 2023. Astrocyte-neuron subproteomes and obsessive-compulsive disorder mechanisms. *Nature*.
1271 616:764–773. doi:10.1038/s41586-023-05927-7.

1272 Stogsdill, J.A., J. Ramirez, D. Liu, Y.H. Kim, K.T. Baldwin, E. Enustun, T. Ejikeme, R.-R. Ji, and C. Eroglu.
1273 2017. Astrocytic neuroligins control astrocyte morphogenesis and synaptogenesis. *Nature*.
1274 551:192–197. doi:10.1038/nature24638.

1275 Sudol, M., and T. Hunter. 2000. NeW Wrinkles for an Old Domain. *Cell*. 103:1001–1004.
1276 doi:10.1016/S0092-8674(00)00203-8.

1277 Sudol, M., K. Sliwa, and T. Russo. 2001. Functions of WW domains in the nucleus. *FEBS Lett.* 490:190–
1278 195.

1279 Sumita, K., Y. Sato, J. Iida, A. Kawata, M. Hamano, S. Hirabayashi, K. Ohno, E. Peles, and Y. Hata. 2007.
1280 Synaptic scaffolding molecule (S-SCAM) membrane-associated guanylate kinase with inverted
1281 organization (MAGI)-2 is associated with cell adhesion molecules at inhibitory synapses in rat
1282 hippocampal neurons. *J. Neurochem.* 100:154–166. doi:10.1111/j.1471-4159.2006.04170.x.

1283 Tan, C.X., D.S. Bindu, E.J. Hardin, K. Sakers, R. Baumert, J.J. Ramirez, J.T. Savage, and C. Eroglu. 2023. δ-
1284 Catenin controls astrocyte morphogenesis via layer-specific astrocyte-neuron cadherin
1285 interactions. *J. Cell Biol.* 222:e202303138. doi:10.1083/jcb.202303138.

1286 Tian, R., X. Wu, T.L. Hagemann, A.A. Sosunov, A. Messing, G.M. McKhann, and J.E. Goldman. 2010.
1287 Alexander Disease Mutant Glial Fibrillary Acidic Protein Compromises Glutamate Transport in
1288 Astrocytes. *J. Neuropathol. Exp. Neurol.* 69:335–345. doi:10.1097/NEN.0b013e3181d3cb52.

1289 Totland, M.Z., C.H. Bergsland, T.A. Fykerud, L.M. Knudsen, N.L. Rasmussen, P.W. Eide, Z. Yohannes, V.
1290 Sørensen, A. Brech, R.A. Lothe, and E. Leithe. 2017. E3 ubiquitin ligase NEDD4 induces
1291 endocytosis and lysosomal sorting of connexin43 to promote loss of gap junctions. *J. Cell Sci.*
1292 jcs.202408. doi:10.1242/jcs.202408.

1293 Varoqueaux, F., G. Aramuni, R.L. Rawson, R. Mohrmann, M. Missler, K. Gottmann, W. Zhang, T.C.
1294 Südhof, and N. Brose. 2006. Neuroligins determine synapse maturation and function. *Neuron*.
1295 51:741–754. doi:10.1016/j.neuron.2006.09.003.

1296 Venkatesh, H.S., T.B. Johung, V. Caretti, A. Noll, Y. Tang, S. Nagaraja, E.M. Gibson, C.W. Mount, J.
1297 Polepalli, S.S. Mitra, P.J. Woo, R.C. Malenka, H. Vogel, M. Bredel, P. Mallick, and M. Monje.
1298 2015. Neuronal Activity Promotes Glioma Growth through Neuroligin-3 Secretion. *Cell*. 161:803–
1299 816. doi:10.1016/j.cell.2015.04.012.

1300 Venkatesh, H.S., L.T. Tam, P.J. Woo, J. Lennon, S. Nagaraja, S.M. Gillespie, J. Ni, D.Y. Duveau, P.J. Morris,
1301 J.J. Zhao, C.J. Thomas, and M. Monje. 2017. Targeting neuronal activity-regulated neuroligin-3
1302 dependency in high-grade glioma. *Nature*. 549:533–537. doi:10.1038/nature24014.

1303 Verkhratsky, A., and M. Nedergaard. 2018. Physiology of Astroglia. *Physiol. Rev.* 98:239–389.
1304 doi:10.1152/physrev.00042.2016.

1305 Wagner, S.A., P. Beli, B.T. Weinert, C. Schölz, C.D. Kelstrup, C. Young, M.L. Nielsen, J.V. Olsen, C.
1306 Brakebusch, and C. Choudhary. 2012. Proteomic analyses reveal divergent ubiquitylation site
1307 patterns in murine tissues. *Mol. Cell. Proteomics MCP*. 11:1578–1585.
1308 doi:10.1074/mcp.M112.017905.

1309 Wang, S., R. Baumert, G. Séjourné, D.S. Bindu, K. Dimond, K. Sakers, L. Vazquez, J.L. Moore, C.X. Tan, T.
1310 Takano, M.P. Rodriguez, N. Brose, L. Bradley, R. Lessing, S.H. Soderling, A.R. La Spada, and C.
1311 Eroglu. 2025. PD-linked LRRK2 G2019S mutation impairs astrocyte morphology and synapse
1312 maintenance via ERM hyperphosphorylation. *BioRxiv Prepr. Serv. Biol.* 2023.04.09.536178.
1313 doi:10.1101/2023.04.09.536178.

1314 Wilson, M.D., S. Sethi, P.J. Lein, and K.P. Keil. 2017. Valid statistical approaches for analyzing sholl data:
1315 Mixed effects versus simple linear models. *J. Neurosci. Methods*. 279:33–43.
1316 doi:10.1016/j.jneumeth.2017.01.003.

1317 Wu, T., E. Hu, S. Xu, M. Chen, P. Guo, Z. Dai, T. Feng, L. Zhou, W. Tang, L. Zhan, X. Fu, S. Liu, X. Bo, and G.
1318 Yu. 2021. clusterProfiler 4.0: A universal enrichment tool for interpreting omics data. *The*
1319 *Innovation*. 2:100141. doi:10.1016/j.xinn.2021.100141.

1320 Xie, H., S. Liu, Y. Fu, Q. Cheng, P. Wang, C.-L. Bi, R. Wang, M.-M. Chen, and M. Fang. 2023. Nuclear access
1321 of DNlg3 c-terminal fragment and its function in regulating innate immune response genes.
1322 *Biochem. Biophys. Res. Commun.* 641:93–101. doi:10.1016/j.bbrc.2022.12.030.

1323 Xie, Y., A.T. Kuan, W. Wang, Z.T. Herbert, O. Mosto, O. Olukoya, M. Adam, S. Vu, M. Kim, D. Tran, N.
1324 Gómez, C. Charpentier, I. Sorour, T.E. Lacey, M.Y. Tolstorukov, B.L. Sabatini, W.-C.A. Lee, and
1325 C.C. Harwell. 2022. Astrocyte-neuron crosstalk through Hedgehog signaling mediates cortical
1326 synapse development. *Cell Rep.* 38:110416. doi:10.1016/j.celrep.2022.110416.

1327 Xu, C., C.D. Fan, and X. Wang. 2015. Regulation of Mdm2 protein stability and the p53 response by
1328 NEDD4-1 E3 ligase. *Oncogene*. 34:281–289. doi:10.1038/onc.2013.557.

1329 Xu, J., Y. Du, J. Xu, X. Hu, L. Gu, X. Li, P. Hu, T. Liao, Q. Xia, Q. Sun, L. Shi, J. Luo, J. Xia, Z. Wang, and J. Xu.
1330 2019. Neuroligin 3 Regulates Dendritic Outgrowth by Modulating Akt/mTOR Signaling. *Front.*
1331 *Cell. Neurosci.* 13:518. doi:10.3389/fncel.2019.00518.

1332 Xu, N., R. Cao, S.-Y. Chen, X.-Z. Gou, B. Wang, H.-M. Luo, F. Gao, and A.-H. Tang. 2024. Structural and
1333 functional reorganization of inhibitory synapses by activity-dependent cleavage of neuroligin-2.
1334 *Proc. Natl. Acad. Sci.* 121:e2314541121. doi:10.1073/pnas.2314541121.

1335 Zhang, Y., K. Chen, S.A. Sloan, M.L. Bennett, A.R. Scholze, S. O'Keeffe, H.P. Phatnani, P. Guarnieri, C.
1336 Caneda, N. Ruderisch, S. Deng, S.A. Liddelow, C. Zhang, R. Daneman, T. Maniatis, B.A. Barres,
1337 and J.Q. Wu. 2014. An RNA-Sequencing Transcriptome and Splicing Database of Glia, Neurons,
1338 and Vascular Cells of the Cerebral Cortex. *J. Neurosci.* 34:11929–11947.
1339 doi:10.1523/JNEUROSCI.1860-14.2014.

1340 Zhang, Y., X. He, X. Meng, X. Wu, H. Tong, X. Zhang, and S. Qu. 2017. Regulation of glutamate
1341 transporter trafficking by Nedd4-2 in a Parkinson's disease model. *Cell Death Dis.* 8:e2574.
1342 doi:10.1038/cddis.2016.454.

1343 Zhou, R., S.V. Patel, and P.M. Snyder. 2007. Nedd4-2 catalyzes ubiquitination and degradation of cell
1344 surface ENaC. *J. Biol. Chem.* 282:20207–20212. doi:10.1074/jbc.M611329200.

1345

1346

1347 **FIGURE LEGENDS**

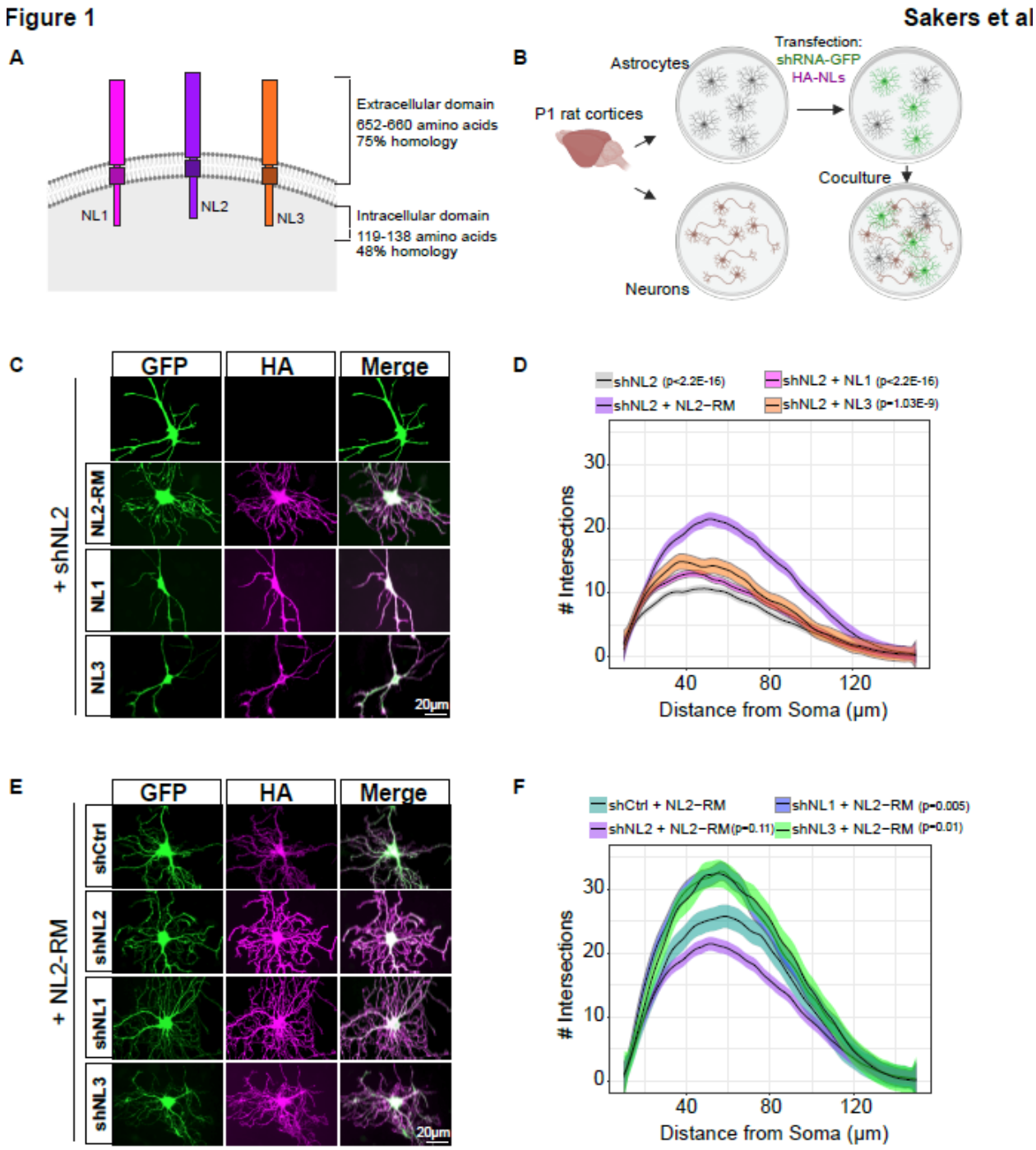

1348

1349 **Figure 1: Astrocytic Neuroligins 1, 2, and 3 have non-redundant roles in**

1350 **morphogenesis.**

1351 A) Cartoon depiction of NLs 1-3. Length and homology refer to mouse sequences.

1352 B) Neuron-astrocyte co-culture method to study astrocyte morphogenesis in vitro. P1 rat
1353 cortices are used to isolate astrocytes and neurons separately to allow for astrocyte-
1354 specific gene manipulation. Astrocytes post-transfection are plated onto neurons for 48h
1355 to allow arborization.

1356 C) Representative images of astrocytes transfected with shNL2 and either: HA-NL2-RM
1357 (Rescue mutant, resistant to shRNA), HA-NL1, or HA-NL3. Scale bars are 20μm.

1358 D) Sholl analysis quantification of conditions shown in C. Linear-mixed model followed
1359 by ANOVA reveals main effect of condition $F(3, 319) = 42.46$, $p < 2.2E-16$. P-values
1360 represent Dunnett's post-hoc with respect to the shNL2+HA-NL2-RM condition. N = 48-
1361 96 cells per condition, across >3 independent culture experiments. See Figure S1C-D
1362 for a comparison of shNL2 to shCtrl astrocytes. Shaded area indicates standard error.

1363 E) Representative images of astrocytes co-transfected with shRNA against either NL1,
1364 NL2, or NL3, and HA-NL2-RM. Scale bars are 20μm.

1365 F) Sholl analysis quantification of conditions in E. Linear-mixed model followed by
1366 ANOVA reveals trending effect of condition $F(3, 311)=15.5$, $p=2.02E-9$. P-values
1367 represent Dunnett's post-hoc with respect to shCtrl+NL2-RM. N = 53-97 cells per
1368 condition, across 3 independent culture experiments. Note that the shNL2 + HA-NL2
1369 data is the same across D and F. Shaded area indicates standard error.

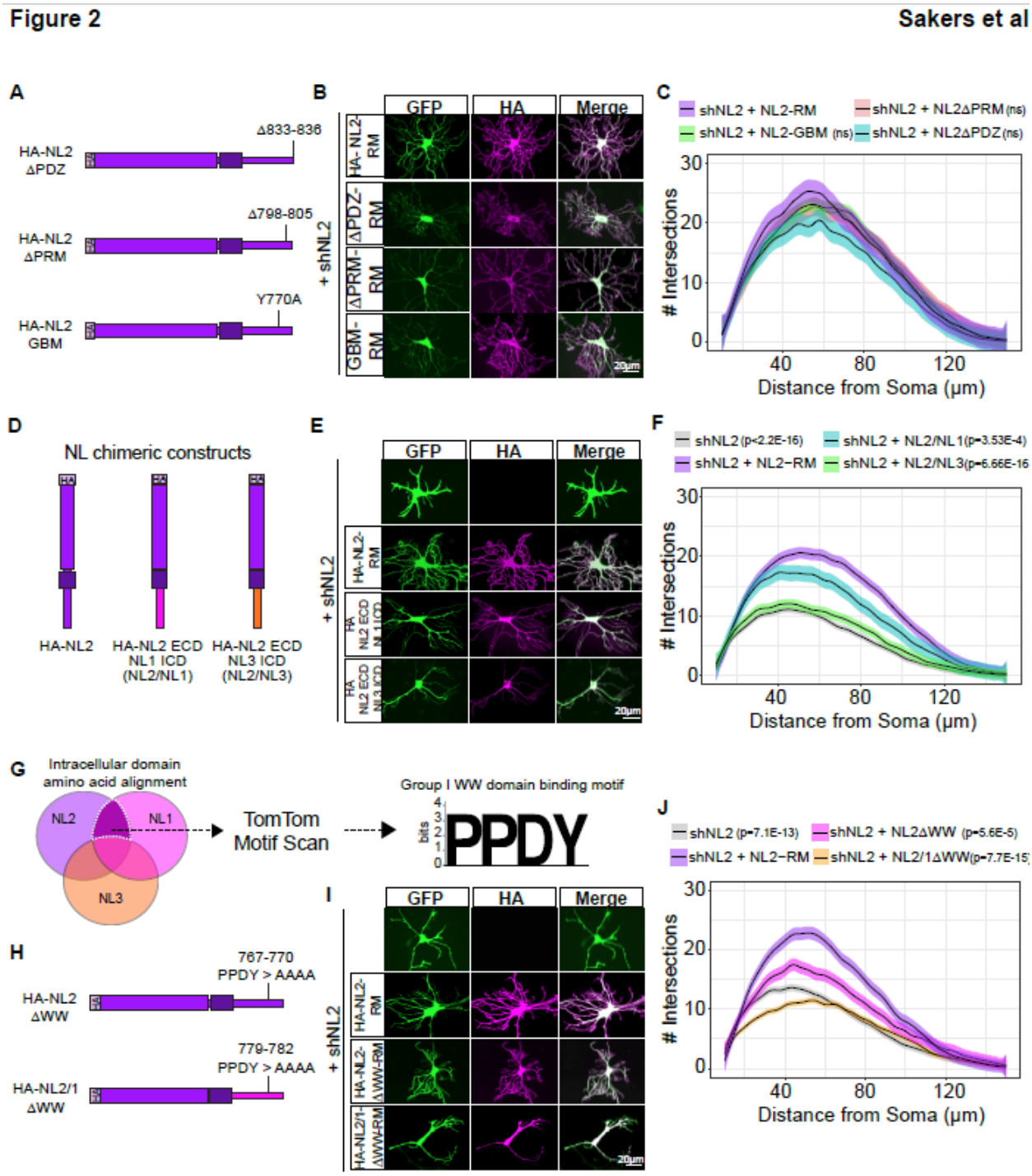

1370

1371 **Figure 2: The intracellular WW-binding motifs of Neuroligins uniquely regulate**

1372 **astrocyte morphology.**

1373 A) Cartoon of NL2 intracellular domain mutants.

1374 B) Representative images of astrocytes co-transfected with shNL2 and either HA-NL2-
1375 RM (Rescue Mutant, resistant to shRNA) or mutants lacking known motifs. Scale bars
1376 are 20μm.

1377 C) Sholl analysis quantification of the conditions in D. Linear-mixed model followed by
1378 ANOVA reveals no effect of condition $F(3, 159)=1.97$, $p=0.12$. NS = not significant in
1379 Dunnett's post-hoc. N=36-46 cells per condition, across 3 independent culture
1380 experiments. Shaded area indicates standard error.

1381 D) Cartoon of NL2-ECD and NL1 or 3 ICD chimeric constructs.

1382 E) Representative images of astrocytes transfected with shNL2 and either HA-NL2-RM
1383 (Rescue mutant, resistant to shRNA), or chimeric proteins: HA-NL2(ECD)-NL1(ICD),
1384 HA-NL2(ECD)-NL3(ICD). Scale bars are 20μm.

1385 F) Sholl analysis quantification of conditions in B. Linear-mixed model followed by
1386 ANOVA reveals the main effect of condition $F(3,356)=38.22$, $p<2.2E-16$. P-values
1387 represent Dunnett's post-hoc with respect to shNL2+NL2-RM. N=57-97 cells per
1388 condition, across 4 independent culture experiments. Shaded area indicates standard
1389 error.

1390 G) Venn diagram depicting the overlap of sequences in NL1, NL2, and NL3 ICDs used
1391 for motif scanning by TomTom. We identified the motif PPDY which is common between
1392 NL1 and NL2 but absent in NL3.

1393 H) Cartoon of NL2ΔWW and NL2/1ΔWW mutant constructs.

1394 I) Representative images of astrocytes transfected with shNL2 and HA-NL2-RM-ΔWW
1395 or shNL2 and HA-NL2/1-ΔWW. Scale bars are 20μm.

1396 J) Sholl analysis quantification of conditions in F. Linear-mixed model ANOVA reveals
1397 the main effect of condition $F(3, 304)=25.76$, $p=7.1E-15$. P-values represent Dunnett's
1398 posthoc with respect to shNL2+NL2-RM. N = 71-84 cells per condition, across 4
1399 independent culture experiments. Shaded area indicates standard error.

1400

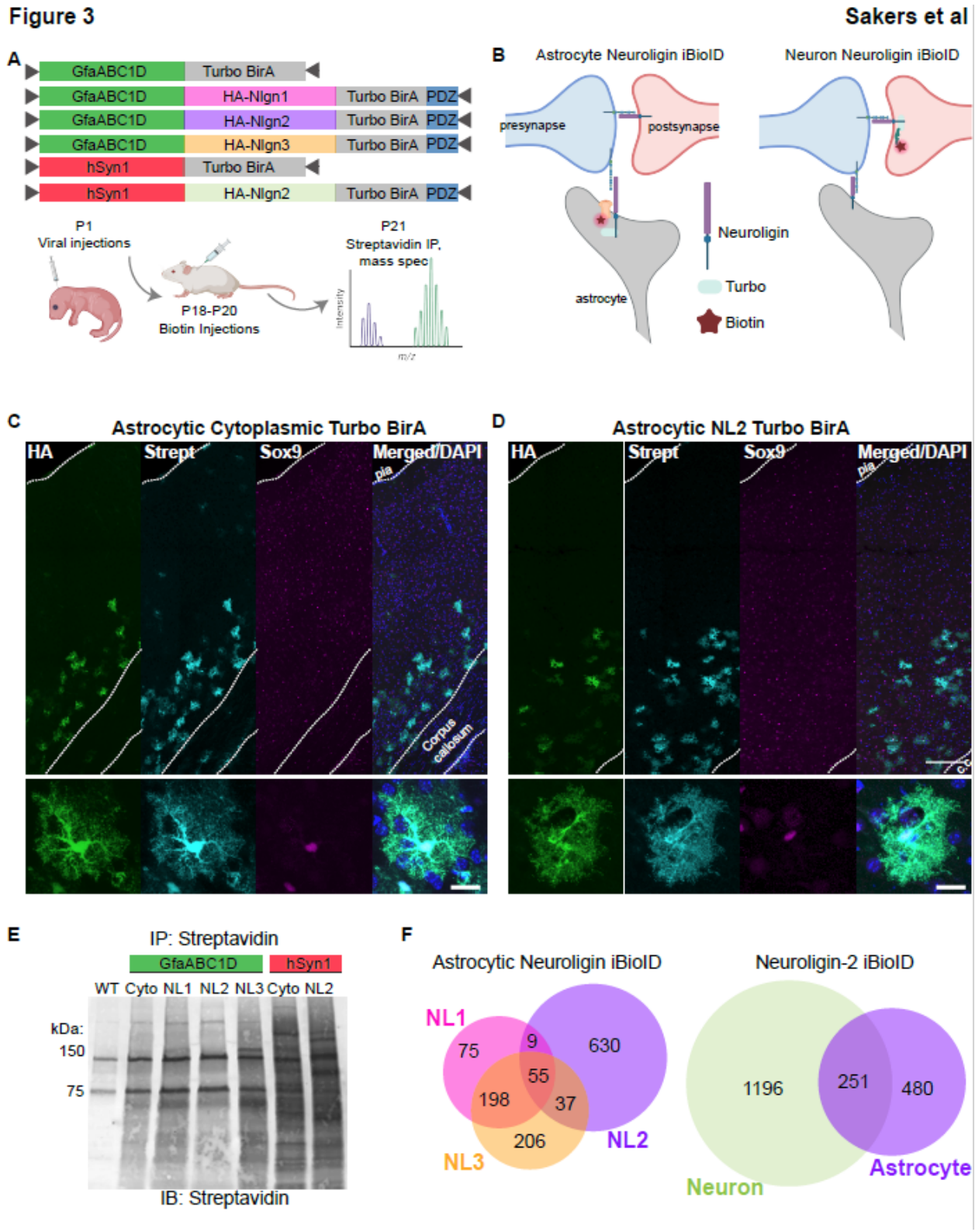

1401

1402 **Figure 3: *In vivo* Neuroligin BioID.**

1403 A) Schematic of AAV constructs and the experimental strategy of in vivo BioID to
1404 identify NL interactome *in vivo*. Each biological replicate contained two pooled cortices,
1405 3 biological replicates per condition.

1406 B) Cartoon depiction of Neuroligin iBioID constructs in astrocytes or neurons.

1407 C-D). Representative cortical images of Astrocytic Turbo BirA (C) or Astrocytic NL2
1408 Turbo BirA (D) injected animals. Stained with Streptavidin-594 (Strept), HA and Sox9 to
1409 determine astrocyte specificity. Scale bars: column image = 100μm; inset = 20μm.

1410 E) Representative western blot of iBioID immunoprecipitation from astrocytic Turbo vs
1411 NL2-Turbo animals demonstrates successful enrichment of biotinylated proteins in
1412 immunoprecipitation. Input is 2% of total cortex homogenate. IP is 15% of the eluate
1413 sample. Prominent bands are expected at approximately 150 and 75kDa which
1414 represent mitochondrial carboxylases(Kirkeby et al., 1993) [blot is overexposed to show
1415 this in the input lanes]. Resulting 'smear' in IP lanes indicated various-sized proteins
1416 that have been biotinylated near the bait protein.

1417 F) Venn diagram of protein interactors across astrocytic NL1, NL2, and NL3 and
1418 astrocytic versus neuronal NL2.

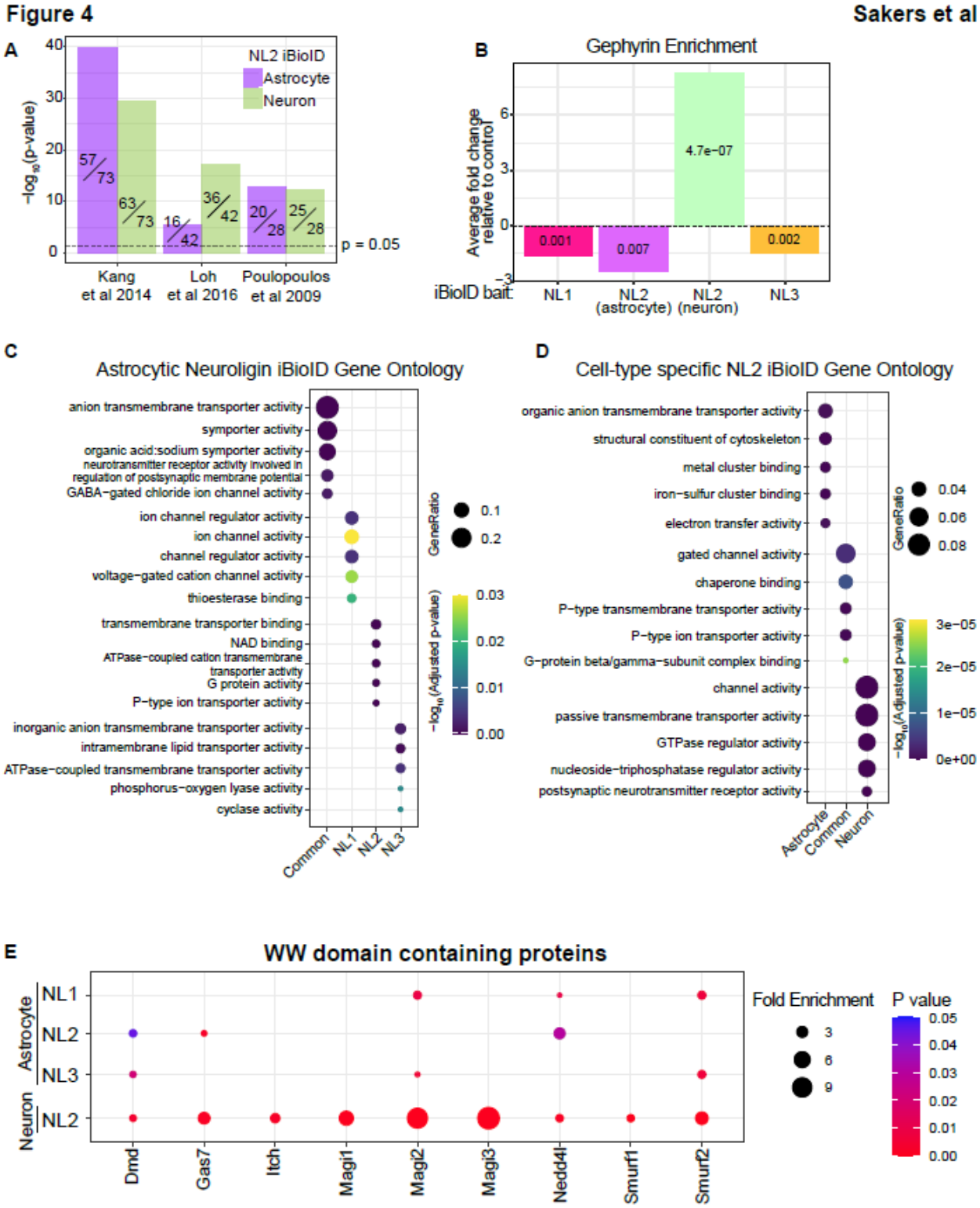

Figure 4: Neuroligin iBioID reveals novel intracellular domain interacting proteins.

1421 A) Enrichment of NL2 iBioID datasets with previously published datasets of NL2-
1422 interacting proteins. P-values are the result of Fisher's exact test. The number on the
1423 bars indicates the number of proteins from appropriate NL2 iBioID that are found in the
1424 published dataset.

1425 B) Gephyrin enrichment with each NL iBioID. Enrichment is defined as fold change bait /
1426 cytosolic control (Turbo BirA). P values are the results of t-tests within each experiment.

1427 C) Top 5 Gene Ontology Biological Processes categories for each NL BioID. Common
1428 indicates proteins found in astrocytic NL1, NL2, and NL3 iBioID. The complete gene
1429 ontology list can be found in Datset S2. GeneRatio indicates number of gene names
1430 (from the input iBioID protein list) in the GO category, out of all gene names in that
1431 category. Input for the analysis was proteins from iBioID lists that were at least 1.5 fold
1432 enriched at a p-value of <0.05, compared to respective controls.

1433 D) Top 5 Gene Ontology Biological Processes categories for each Neuronal or
1434 Astrocytic NL2 BioID. Common indicates proteins found in both astrocytic NL2 and
1435 neuronal NL2 iBioID. The complete gene ontology list can be found in Dataset S2.
1436 GeneRatio indicates number of gene names (from the input iBioID protein list) in the GO
1437 category, out of all gene names in that category. Input for the analysis was proteins
1438 from iBioID lists that were at least 1.5 fold enriched at a p-value of <0.05, compared to
1439 respective controls.

1440 E) All identified WW-binding protein interactors in iBioID experiments. Fold change is
1441 the enrichment of the interaction with the bait compared to cytosolic Turbo BirA alone,
1442 per cell type. P-value represents a two-tailed T-test compared to soluble Turbo BirA, per

1443 cell type. Input for the analysis was proteins from iBioID lists that were at least 1.5 fold

1444 enriched at a p-value of <0.05, compared to respective controls.

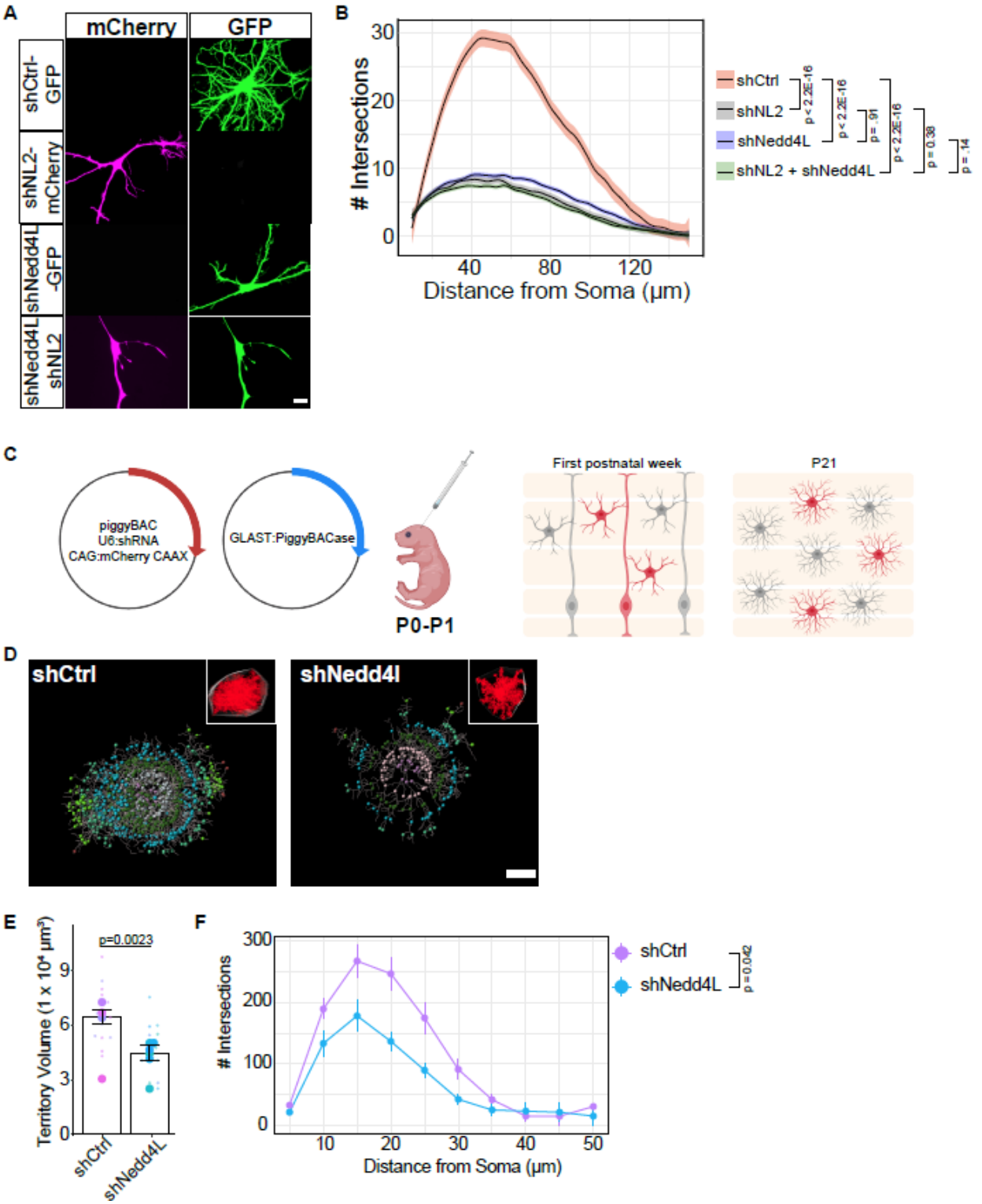
A
mCherry
GFP
shCtrl-GFP
shNL2-mCherry
shNedd4L-GFP
shNedd4L shNL2
B
Intersections
Distance from Soma (µm)
shCtrl
shNL2
shNedd4L
shNL2 + shNedd4L
p < 2.2E-16
p < 2.2E-16
p = .91
p < 2.2E-16
p = 0.38
p = .14
C
piggyBAC
U6:shRNA
CAG:mCherry CAAX
GLAST:PiggyBACase
P0-P1
First postnatal week
P21
D
shCtrl
shNedd4l
E
Territory Volume (1 x 10⁴ µm³)
p=0.0023
shCtrl
shNedd4L
F
Intersections
Distance from Soma (µm)
shCtrl
shNedd4L
p=0.042

1445

1446 **Figure 5: WW domain-containing proteins are necessary for astrocyte**
1447 **morphogenesis in vitro.**

1448 A) Representative images of astrocytes transfected with either a control shRNA
1449 (scrambled NL2 shRNA), an shRNA targeting Nedd4l (also expressing GFP) or shNL2
1450 (also expressing mCherry), or in combination. Astrocytes are cultured on top of neurons
1451 (not labeled). Scale bar is 20μm.

1452 B) Sholl analysis of the conditions in A. Linear-mixed model ANOVA reveals the main
1453 effect of condition $F(3, 332)=217.36$, $p<2.2E-16$. P-values on the graph represent
1454 Tukey's posthoc comparison to shCtrl. N = 60-100 cells per condition, across 4
1455 independent culture experiments. Shaded area indicates standard error.

1456 C) Cartoon of postnatal astrocyte labeling by electroporation (PALE). Two plasmids
1457 (U6:shRNA and CAG:mCherry CAAX flanked by piggyBAC transposons, and GLAST:
1458 piggyBACase transposase) are electroporated into late P0 or early P1 mouse lateral
1459 ventricles. Brains are collected at P21 and stained for mCherry to visualize astrocyte
1460 territories.

1461 D) Imaris reconstructions of *in vivo* astrocyte territory volumes (inset) and 3D Sholl
1462 analysis of mouse cortical astrocytes. 'Filament' cytoskeletal structure is shown with
1463 grey lines, while spheres indicate 3D Sholl concentric circles [different colors indicate
1464 different distances from the nucleus]. Scale bars = 10μm.

1465 E) Territory volume super plot quantification of the conditions in C. Large dots on graph
1466 = average per animal. Smaller dots = individual cells. Data were analyzed using a
1467 nested ANOVA; main effect of condition, $F(1, 8) = 11.95$, $p=0.0023$. The same cells

1468 were measured for territory volume and Sholl analysis. N=14-18 cells across 4-7
1469 animals (biological replicates) per condition. Layer identity of cells imaged: shCtrl [L2/3:
1470 1, L4: 10, L5/6: 7]; shNedd4l [L2/3: 2, L4: 8, L5/6: 4]

1471 F) 3D Sholl analysis. Linear mixed model ANOVA $F(1,9)=5.59$, $p=0.0424$. The same
1472 cells were measured for territory volume and Sholl analysis. N=14-18 cells across 4-7
1473 animals (biological replicates) per condition. Error bars indicate standard error.

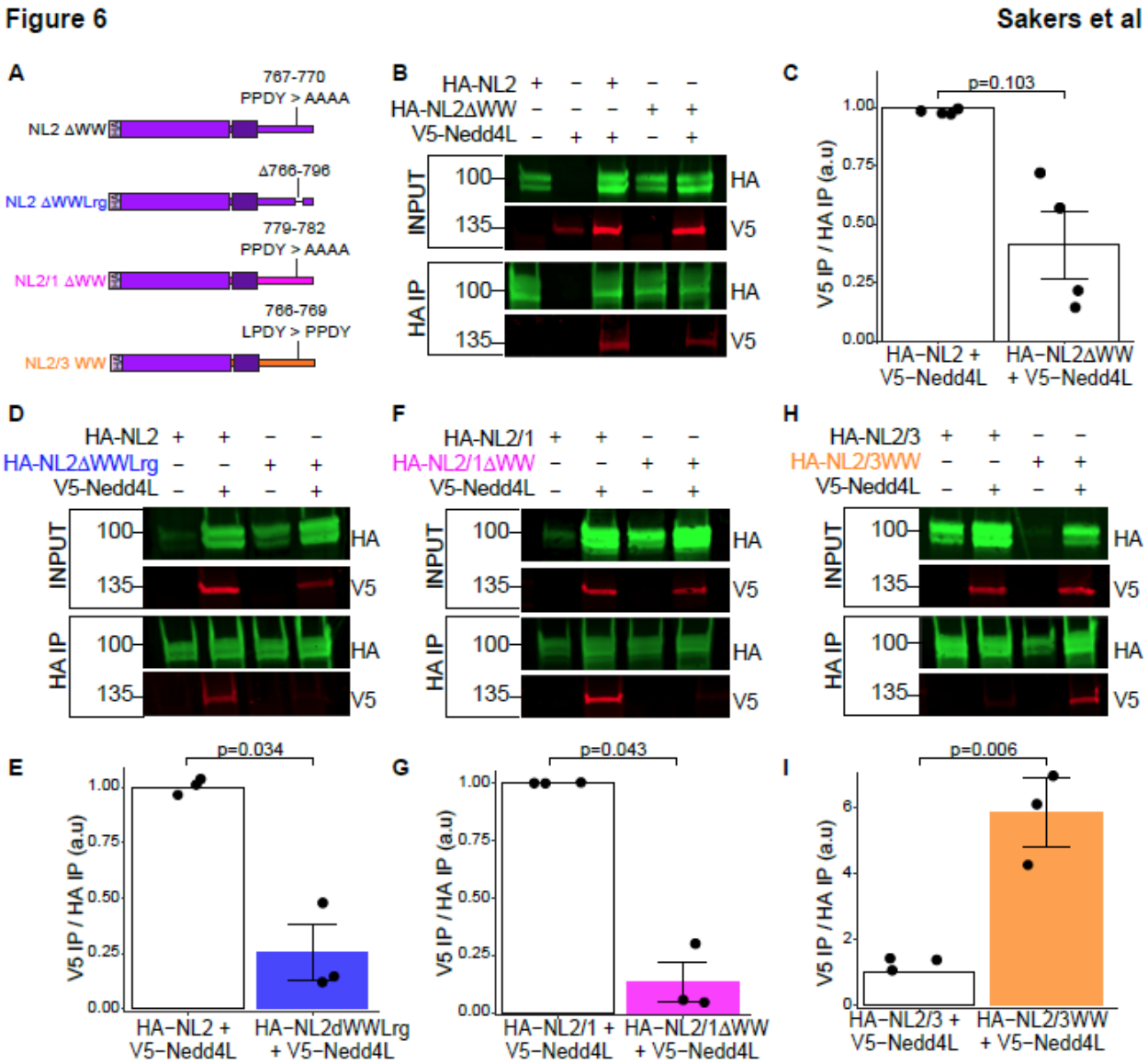

Figure 6: Nedd4l binding to Neuroligins is modulated by intracellular PPxY motifs

A) Cartoon of NL2 and NL2-ICD chimeric constructs. Numbers indicate amino acid positions in mouse sequence.

B) Western blots from HEK cell lysates transfected with HA-NL2 or HA-NL2ΔWW with or without V5-Nedd4l constructs. Co-immunoprecipitation (IP) of V5-Nedd4l was detected with NL2-HA constructs using Li-Cor fluorescent imaging.

1481 C) Densitometry quantification of IP signal from conditions in B. N=4 biological
1482 replicates. P-values represent results of paired, Student's t-test.

1483 D) Western blots from HEK cell lysates transfected with HA-NL2 or HA-NL2ΔWWLrg
1484 (Deletion of amino acids 766-796) with or without V5-Nedd4l constructs. Co-
1485 immunoprecipitation (IP) of V5-Nedd4l was detected with NL2-HA constructs using Li-
1486 Cor fluorescent imaging.

1487 E) Densitometry quantification of IP signal from conditions in D. N=3 biological
1488 replicates (independent culture experiments). P-values represent results of paired,
1489 Student's t-test.

1490 F) Western blots from HEK cell lysates transfected with HA-NL2/1 or HA-NL2/1ΔWW
1491 with or without V5-Nedd4l constructs.

1492 G) Densitometry quantification of IP signal from conditions in F. N=3 biological
1493 replicates. P-values represent results of paired, Student's t-test.

1494 H) Western blots from HEK cell lysates transfected with HA-NL2/3 or HA-NL2/3-WW
1495 with or without V5-Nedd4l constructs.

1496 I) Densitometry quantification of IP signal from conditions in H. N=3 biological replicates.
1497 P-values represent results of paired, Student's t-test.

1498 (B, D, F, H) All western blots were run at least 3 times with independent samples. Note
1499 that Nedd4l (V5) blots were run separately (eluate divided evenly) to avoid bleed-
1500 through from the strong HA signal.

1501

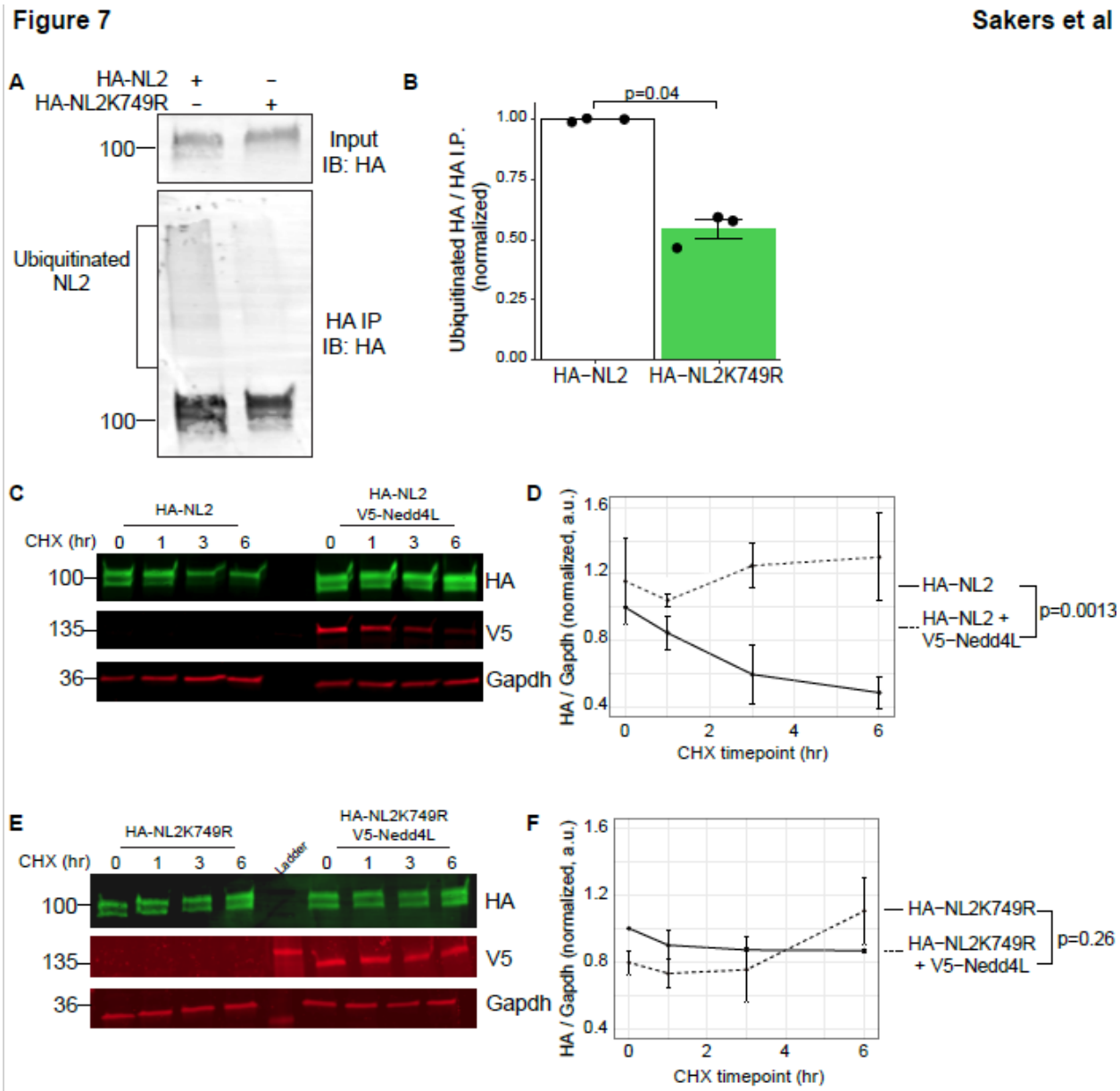

Figure 7: Nedd4l stabilizes Neuroligin-2 via ubiquitination at K749R.

A) Western blot from rat primary astrocyte cell lysates and HA-NL2 IPs shows NL2 is ubiquitinated in astrocytes, which is lost when NL2 K749 is mutated to arginine (K749R). Input is 2% of total lysate.

1507 B) Quantification of HA ubiquitination signal from conditions in A. The ubiquitinated HA
1508 bands >100kDa were quantified via densitometry and normalized to the HA IP band
1509 (~100kDa) per biological replicate. N=3 biological replicates (independent culture
1510 experiments). P-values represent results of paired, Student's t-test.

1511 C) Western blots from HEK cell lysates transfected with HA-NL2 or HA-NL2 + V5-
1512 Nedd4l and treated with CHX. Numbers above the blot indicate hours after CHX
1513 treatment.

1514 D) Quantification of the conditions in B. Samples were collected on N=3 independent
1515 samples. Two-way ANOVA reveals main effect of condition $F(1, 16)=15.018$,
1516 $p=0.00134$, with no significant effect of time-point $F(3, 16)=0.41$, $p=0.74827$ or
1517 interaction $F(3, 16)=2.242$, $p=0.123$.

1518 E) Western blots from HEK cell lysates transfected with HA-NL2K749R or HA-
1519 NL2K749R + V5-Nedd4l and treated with CHX. Numbers above the blot indicate hours
1520 after CHX treatment.

1521 F) Quantification of the conditions in D. Samples were collected on N=3 independent
1522 samples. Two-way ANOVA reveals no significant effect of condition $F(1, 16)=1.392$,
1523 $p=0.255$, time-point $F(3, 16)=1.681$, $p=0.211$ or interaction $F(3, 16)=2.328$, $p=0.113$.

1524

Figure 8

Sakers et al

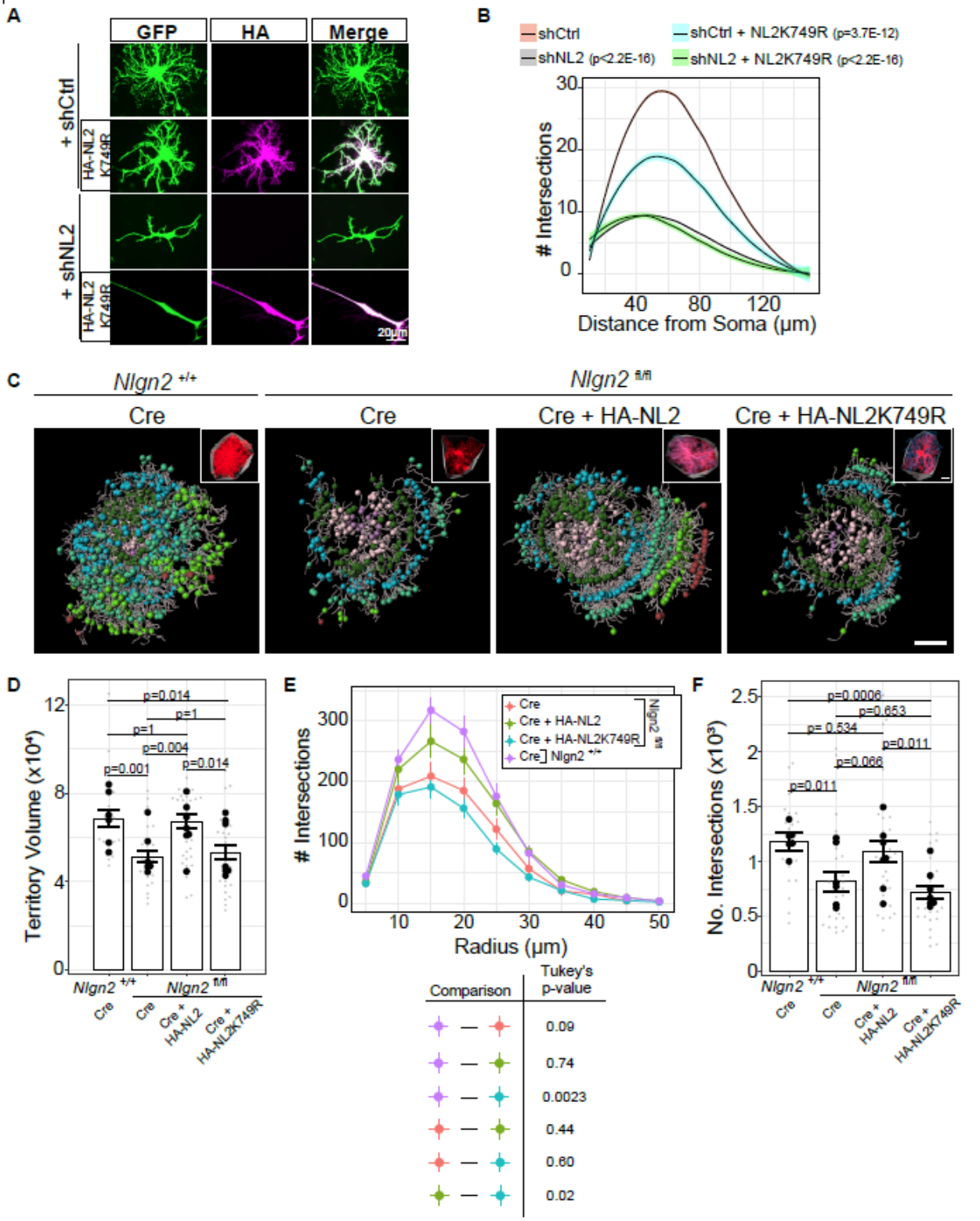

1525

1526 **Figure 8: Neuroligin-2 ubiquitination at K749 is critical for astrocyte**
1527 **morphogenesis.**

1528 A) Representative images of astrocytes transfected with either shCtrl or shNL2 with or
1529 without HA-NL2K749R expression. Scale bars are 20μm.

1530 B) Sholl analysis quantification of images in J. Linear-mixed model ANOVA reveals the
1531 main effect of condition $F(3, 284)=103.14$, $p<2.2E-16$. P-values represent Dunnett's
1532 posthoc with respect to shCtrl. N = 62-80 cells per condition, across 3 independent
1533 culture experiments. Shaded area indicates standard error.

1534 C) Representative images of reconstructed astrocytes. 'Filament' cytoskeletal structure
1535 is shown with grey lines, while spheres indicate 3D Sholl concentric circles [different
1536 colors indicate different distances from the nucleus]. Insets show the astrocyte signal
1537 [tdTomato signal in red; HA signal in cyan] with the convex hull [grey surface lines].
1538 Scale bar = 10μm.

1539 D) Territory volume super plot quantification of the conditions in C. Large black dots on
1540 graph = average per animal. Smaller grey dots = individual cells. Data were analyzed
1541 using Kruskal-Wallis rank sum test: $\chi^2 = 19.5$, df=3, p=0.00013. P-values on the graph
1542 are results of the Wilcoxon rank sum post hoc tests with Holm-Šídák multiple
1543 comparison correction. The same cells were measured for territory volume and Sholl
1544 analysis. N=21-33 cells across 6-7 animals (biological replicates) per condition.

1545 E) 3D Sholl analysis. Linear mixed model ANOVA $F(3, 102)=5.08$, p=0.0025. P-values
1546 in the table represent Tukey's post hoc tests. The same cells were measured for

1547 territory volume and Sholl analysis. N=21-33 cells across 6-7 animals (biological
1548 replicates) per condition. Error bars represent standard error.

1549 F) Total number of intersections (No. Intersections, y-axis) from cells in Sholl Analysis
1550 (E). Large black dots on graph = average per animal. Smaller grey dots = individual
1551 cells. Data were analyzed using Kruskal-Wallis rank sum test: $\chi^2 = 19.247$, df=3,
1552 p=0.000243. P-values on the graph are results of the Wilcoxon rank sum post hoc tests
1553 with Holm-Šídák multiple comparison correction. The same cells were measured for
1554 territory volume and Sholl analysis. N=21-33 cells across 6-7 animals (biological
1555 replicates) per condition.

1556

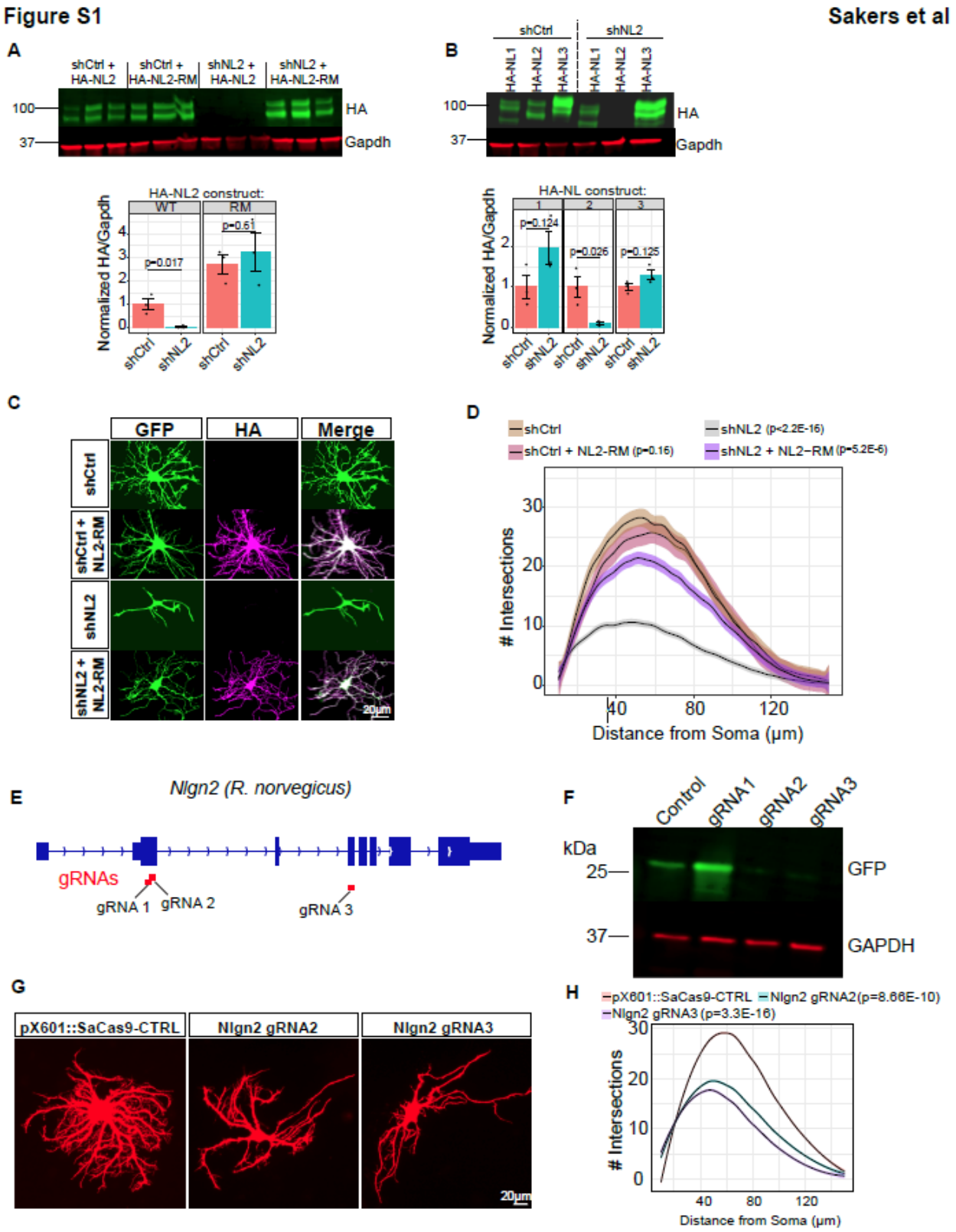

Supplemental Figure 1:

1559 A) Western blots of HA-NL2 expressed in HEK293T cells. HEK293T cells were
1560 transfected with shCtrl or shNL2, and either HA-NL2 or HA-NL2-RM (Rescue mutant) to
1561 assess the efficacy of shNL2. HA and Gapdh bands were quantified via densitometry.
1562 HA was normalized to Gapdh to produce the graph below. HA-NL2 is reduced by >90%
1563 with shNL2. shNL2 has no effect on the HA-NL2-RM construct. Statistics are the result
1564 of a Student's t-test.

1565 B) Western blots of HA-NL2 expressed in HEK293T cells. HEK293T cells were
1566 transfected with shCtrl or shNL2 and either HA-NL1, HA-NL2 or HA-NL3 to assess the
1567 specificity of shNL2. HA and Gapdh bands were quantified via densitometry. HA was
1568 normalized to Gapdh to produce the graph below. HA-NL2 is specifically targeted by
1569 shNL2. shNL2 results in non-significant increases in HA-NL1 and HA-NL3. Statistics are
1570 the result of a Student's t-test.

1571 C) Representative images of astrocytes cultured on neurons. Astrocytes were
1572 transfected with either shCtrl or shNL2, alone or with HA-NL2-RM (Rescue mutant).

1573 D) Sholl analysis of images represented in A. Linear-mixed model followed by ANOVA
1574 reveals the main effect of condition $F(3, 286)=75.01$, $p<2.2E-16$. P-values represent
1575 post hoc Dunnett's comparison to shCtrl. N = 53-96 cells per condition, across 3
1576 biological replicates (independent culture experiments). Shaded area indicates standard
1577 error.

1578 E) *Nlgn2* sequence illustrating location of the gRNAs using in D and E.

1579 F) Western blot of GFP translation assay. The target sequence of the gRNAs is cloned
1580 upstream and in-frame with GFP. gRNAs are co-expressed and then lysates are

1581 collected and run in equal protein load on an SDS-PAGE. The western blot was probed
1582 for GFP and GAPDH, for normalization.

1583 G) Representative images of astrocytes cultured on neurons. Astrocytes were
1584 transfected with pX601 (U6 gRNA GfaABC1D Cas9 T2A mCherry) prior to culturing on
1585 neurons.

1586 H) Sholl analysis of images represented in C. Linear-mixed model followed by ANOVA
1587 reveals the main effect of condition $F(2, 185) = 37.0175$, $p=3E-14$. P-values represent
1588 post hoc Tukey's comparison to shCtrl. N = 40 cells per condition, across 3 biological
1589 replicates (independent culture experiments). Shaded area indicates standard error.

Figure S2 **Sakers et al**

A

```
NL1-ICD    1 YYKKDKRRHDVHRRCSPQRTTT-NDL-----------THAPEEEIMSLQMKHTDLDHECE
NL2-ICD    1 YYKRDRRQELRCRRLSPPGGSGSGVPGGGPLLPTAGRELPPEEELVSLQLKRGG----GV
NL3-ICD    1 YYRKDKRRQEPLRQPSPQRGTGAPEL-----------GTAPEEELAALQLGPTH-HECE
                                 *
NL1-ICD   49 SIHPHEVVLRTACPPDYTLAMRRSPDDIPLMTPNTITMIPNTI-----PGIQPLHTFNTF
NL2-ICD   57 GADPAEA-LRPACPPDYTLALRRAPDDVPLLAPGALTLLPSGLGPPPPPPPPSLHPFGPF
NL3-ICD   48 AGPPHDT-LRLTALPDYTLTLRRSPDDIPLMTPNTITMIPNSL-----VGLQTLHPYNTF

NL1-ICD  104 TGGQNNTLPHPHPHPHSHSTTRV
NL2-ICD  116 PPPPPTATSHNNTLPHPHSTTRV
NL3-ICD  102 AAGFNST-----GLPHSHSTTRV
```

*Gephryin binding residue
Proline-rich motif
PDZ-binding motif
Type I WW binding motif

B

Surface Staining (No detergent)

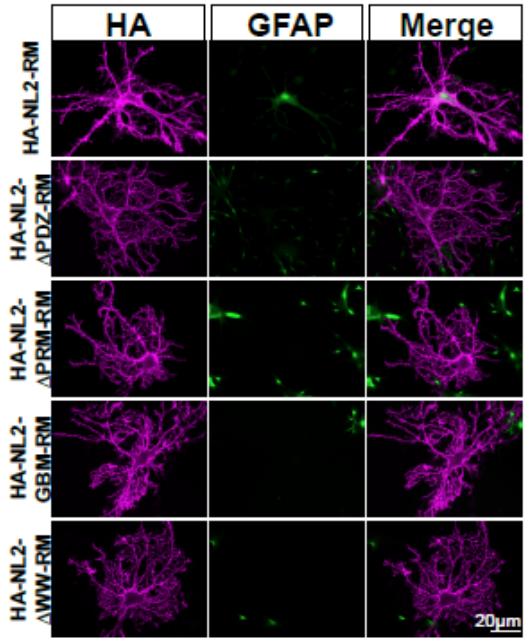

Supplemental Figure 2:

A) Mouse Neuroligin intracellular domain alignment, highlighting relevant protein sequence motifs.

B) Representative images of surface-stained astrocyte/neuron co-cultures. Cells were fixed with cold 4% PFA for 5 minutes, and triton was omitted from blocking steps to avoid intracellular staining. GFAP was used as a negative control. HA (magenta) signal shows membrane localization as expected. GFAP signal is largely absent in the absence of detergent.

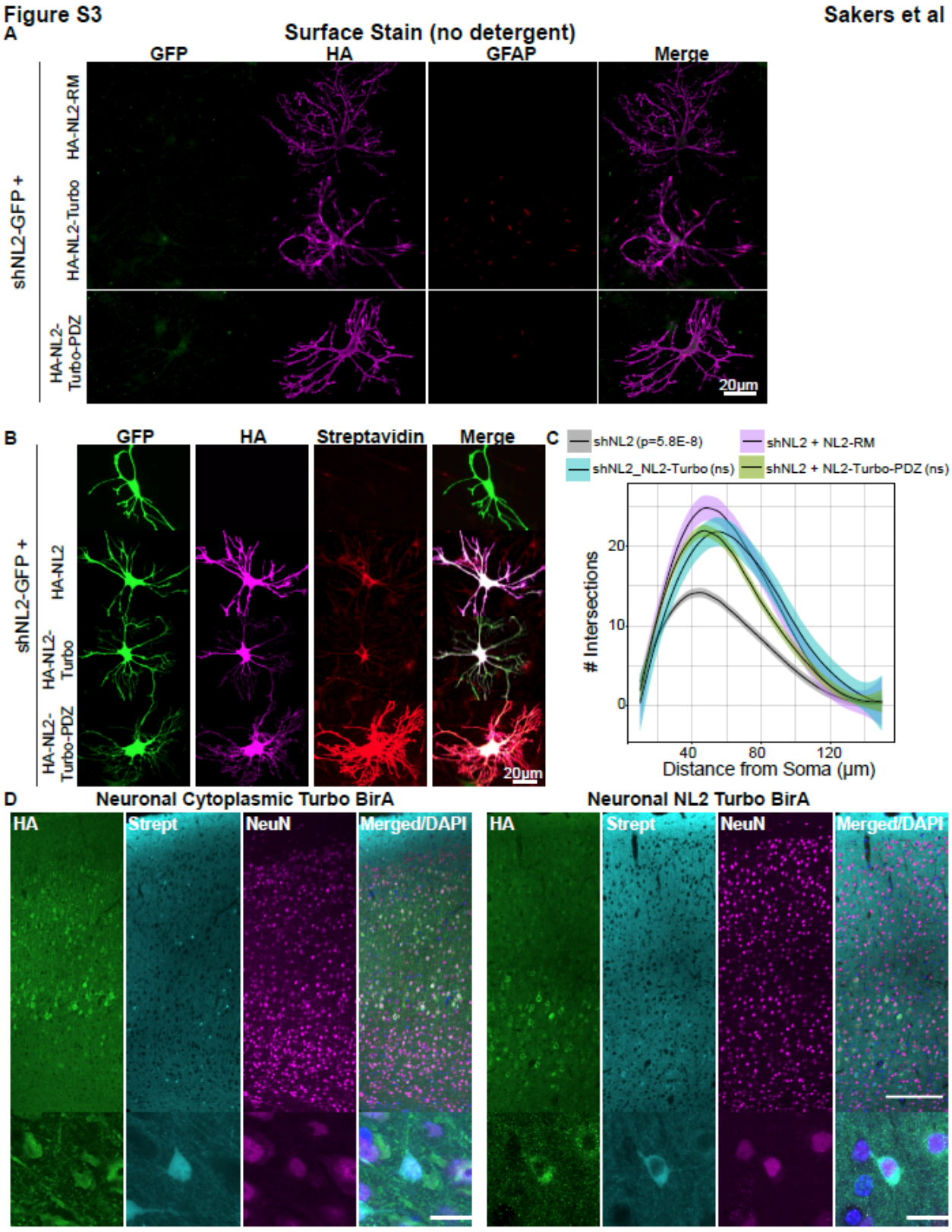

Supplemental Figure 3:

1601 A) Representative images of surface-stained astrocyte/neuron co-cultures. Cells were
1602 fixed with cold 4% PFA for 5 minutes, and triton was omitted from blocking steps to
1603 avoid intracellular staining. GFP and GFAP were used as negative controls. HA
1604 (magenta) signal shows membrane localization as expected.

1605 B) Representative images demonstrating effective biotinylation (Streptavidin Alexa 594,
1606 red) in HA-NL2-Turbo-PDZ but not in HA-NL2 (negative control) or HA-NL2-Turbo.
1607 Experiments were performed at least twice with at least 20 cells per condition.

1608 C) Sholl analysis quantification of images in B. Linear-mixed model reveals the main
1609 effect of condition, $F(1,3)=11.01$, $p=1.4E-6$. P-values represent Dunnett's post-hoc with
1610 respect to shNL2 + NL2-RM. NS = not significant in Dunnett's. N = 14-56 cells across 3
1611 biological replicates (independent culture experiments). Shaded area indicates standard
1612 error.

1613 D). Representative cortical images of Neuronal Turbo BirA injected animals. Stained
1614 with Streptavidin-594 (Strept), HA and NeuN to determine neuronal specificity. Scale
1615 bars: column image = 100μm; inset = 20μm.

Figure S4 **Sakers et al**

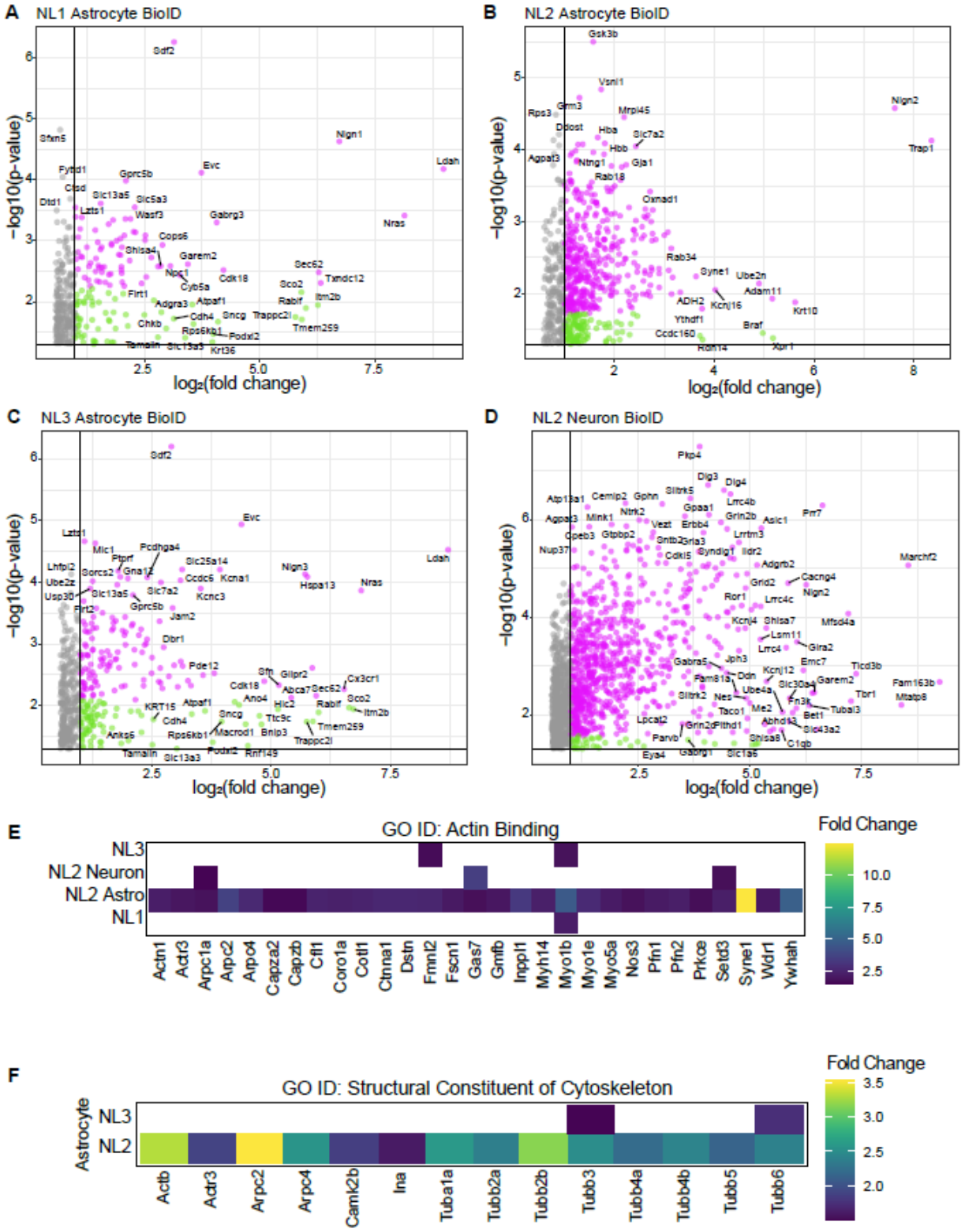

Supplemental Figure 4:

1618 A-D) Volcano plots of all proteins identified in the iBioID experiments. Pink dots indicate
1619 proteins enriched over cytoplasmic control with a fold change > 1.5 and an FDR-
1620 corrected p-value < 0.05. Green dots indicate proteins enriched over cytoplasmic control
1621 with a fold change > 1.5 and a p-value < 0.05.

1622 E-F) Expression of genes related to Actin Binding (E) or Structural Constituent of
1623 Cytoskeleton (F) from Gene Ontology analysis of iBioID shows that astrocytic NL2
1624 significantly interacts with cytoskeletal genes, compared to astrocyte NL1/NL3 or
1625 neuronal NL2.

1626

Figure S5 Sakers et al

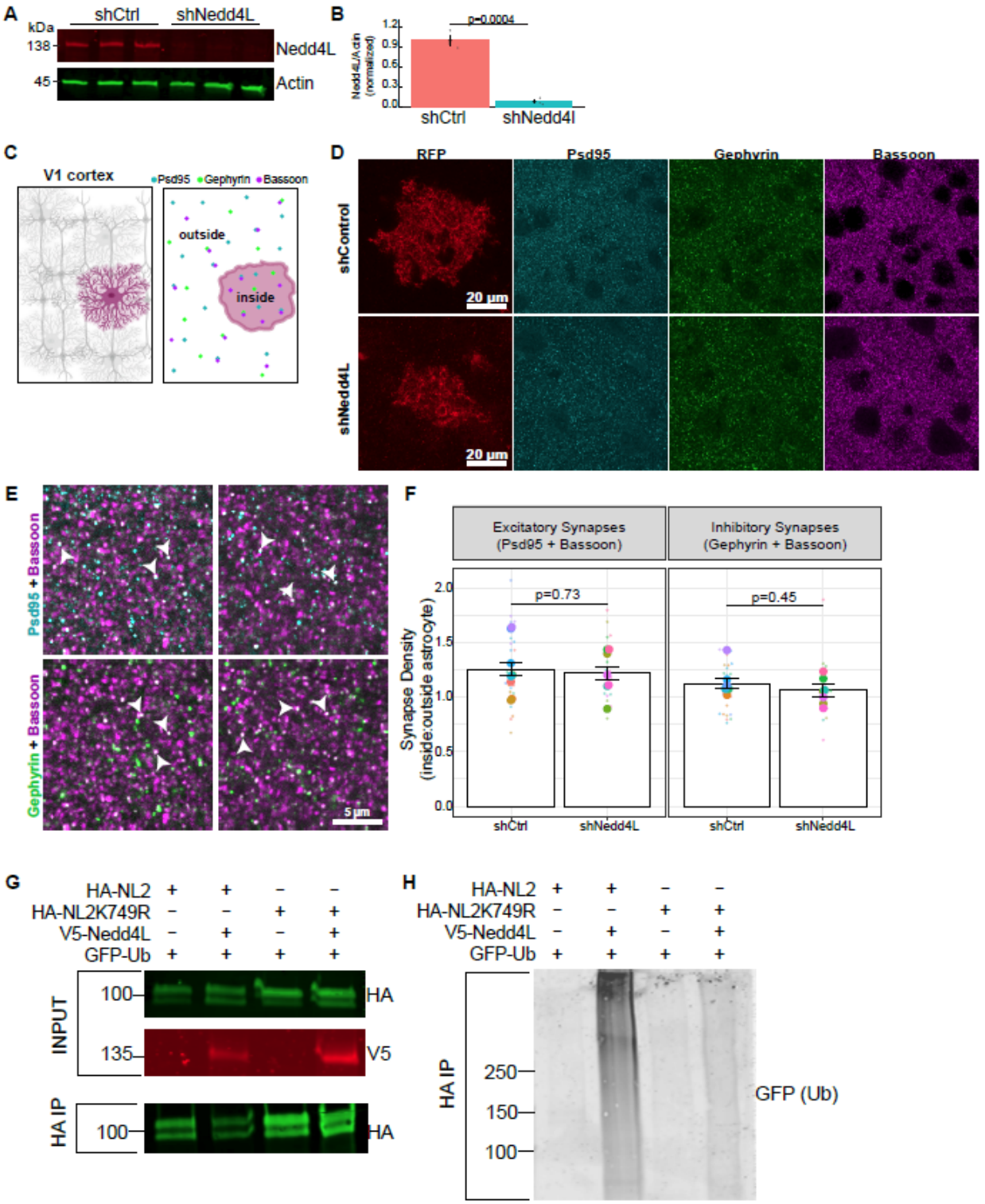

Supplemental Figure 5:

1629 A) Western blots of astrocytes treated with lentivirus expressing shCtrl (scrambled
1630 shRNA) or shNedd4l.

1631 B) Densitometry quantification [ImageJ]. The p value represents the results of the
1632 Student's t-test.

1633 C) Cartoon of synapse analysis. Sparsely labeled astrocytes (shControl mCherry CAAX;
1634 shNedd4l mCherry CAAX) were imaged in P21 mouse V1 cortex. Synapses
1635 (colocalized Psd95 + Bassoon [excitatory synapses] or Gephyrin + Bassoon [inhibitory
1636 synapses]) were quantified within the astrocyte territory (inside) and outside of the
1637 astrocyte territory (outside).
1638 D) Representative images of mCherry-labeled astrocytes (RFP antibody), with Psd95
1639 (cyan), Gephyrin (green), Bassoon (magenta) staining.

1640 E) Magnified image showing colocalized synapse puncta for excitatory (Psd95 +
1641 Bassoon), and inhibitory (Gephyrin and Bassoon) synapses. Colocalized puncta are
1642 shown in white, with examples indicated with arrows.

1643 F) Quantification of synapse density within labeled astrocyte to the outside unlabeled
1644 astrocyte territory. Large dots represent individual animals, with small dots representing
1645 each image from an animal. P-values indicate main effect of linear mixed effects
1646 ANOVA. Excitatory synapses: $F(1,13) = 0.12$, $p=0.73$. Inhibitory synapses: $F(1,13) =$
1647 0.61, $p=0.45$. 7-8 animals were used per condition, with 4-8 images taken per animal.

1648 G-H) Western blot from HEK cell lysates and HA-NL2 IPs (G) shows NL2 ubiquitination
1649 (H) with Nedd4l overexpression, which is substantially reduced when NL2 is mutated at

1650 K749. GFP-tagged ubiquitin was overexpressed in these cells to visualize ubiquitinated

1651 NL2 in the immunoprecipitation.

1652 **Supplemental Dataset 1: In vivo BioID results.** All proteins significantly enriched in
1653 Astrocytic NL1 (sheet 1), Astrocytic NL2 (sheet 2), Astrocytic NL3 (sheet 3), and
1654 Neuronal NL (sheet 4) iBioID compared to Astrocytic TurboID alone.

1655 **Supplemental Dataset 2: iBioID Gene Ontology output.** All biological process gene
1656 ontology results. Column 1 indicates the iBioID list to which the categories correspond
1657 to.

1658 **Supplemental Table 1: Detailed statistical analyses for each figure panel.**